Article

Mechanistic Insights into the Oxygen Atom Transfer Reactions by Nonheme Manganese Complex: A Computational Case Study on the Comparative Oxidative Ability of Manganese-Hydroperoxo vs High-Valent Mn^{IV}=O and Mn^{IV}−OH Intermediates

Ravi Kumar, Bhawana Pandey, Akta Singh, and Gopalan Rajaraman*

Read Online

ACCESS | Metrics & More | Article Recommendations | Supporting Information

ABSTRACT: Understanding the comparative oxidative abilities of high-valent metal-oxo/hydroxo/hydroperoxo species holds the key to robust biomimic catalysts that perform desired organic transformations with very high selectivity and efficiency. The comparative oxidative abilities of popular high-valent iron-oxo and manganese-oxo species are often counterintuitive, for example, oxygen atom transfer (OAT) reaction by [(Me$_2$EBC)Mn^{IV}−OOH]$^{3+}$, [(Me$_2$EBC)Mn^{IV}−OH]$^{3+}$, and [(Me$_2$EBC)Mn^{IV}=O]$^{2+}$ (Me$_2$EBC = 4,11-dimethyl-1,4,8,11-tetraazabicyclo[6.6.2]hexadecane) shows extremely high reactivity for Mn^{IV}−OOH species and no reactivity for Mn^{IV}−OH and Mn^{IV}=O species toward alkyl/aromatic sulfides. Using a combination of density functional theory (DFT) and ab initio domain-based local pair natural orbital coupled-cluster with single, double, and perturbative triples excitation (DLPNO-CCSD(T)) and complete-active space self-consistent field/N-electron valence perturbation theory second order (CASSCF/NEVPT2) calculations, here, we have explored the electronic structures and sulfoxidation mechanism of these species. Our calculations unveil that Mn^{IV}−OOH reacts through distal oxygen atom with the substrate via electron transfer (ET) mechanism with a very small kinetic barrier (16.5 kJ/mol), placing this species at the top among the best-known catalysts for such transformations. The Mn^{IV}−OH and Mn^{IV}=O species have a much larger barrier. The mechanism has also been found to switch from ET in the former to concerted in the latter, rendering both unreactive under the tested experimental conditions. Intrinsic differences in the electronic structures, such as the presence and absence of the multiconfigurational character coupled with the steric effects, are responsible for such variations observed. This comparative oxidative ability that runs contrary to the popular iron-oxo/hydroperoxo reactivity will have larger mechanistic implications in understanding the reactivity of biomimic catalysts and the underlying mechanisms in PSII.

Proximal Attack (P)
Distal Attack (D)
Large steric hindrance
Small steric hindrance
ET
Reactivity Order: Mn^{IV}-OOH > Mn^{IV}=O > Mn^{IV}-OH
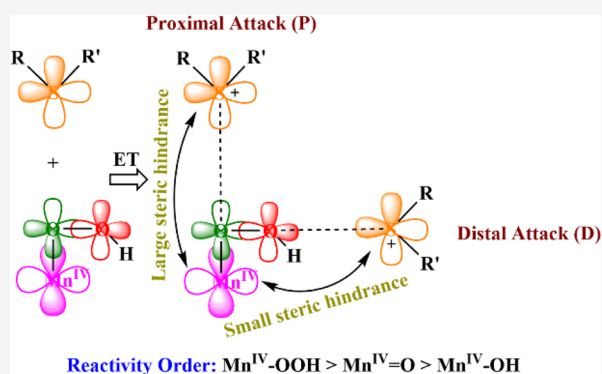
INTRODUCTION

Heme and nonheme high-valent metal-oxo and metal-hydroxo species are proposed as key intermediates in various biological processes such as photosystem-II,[1] peroxidases,[2] catalases,[3] bleomycin,[4] and naphthalene dioxygenase.[5] These species can also oxygenate many organic substrates and are of high relevance to pharmaceutical industries.[5−7] These metalloenzymes have inspired a range of biomimetic studies, as these are expected to shed light on complex biological processes and will also help us to design new catalysts with increased efficiency and selectivity. Recently, metal-hydroperoxo species are also gaining significant attention as these species are a precursor in various chemical and biotransformation reactions.[8,9] These species are predicted to be a better oxidant than its corresponding oxo and hydroxo species. With this motive, the synthetic effort to prepare complexes with high-valent metal-oxo, metal-peroxo, and metal-hydroperoxo units that mimic the catalytic activity of metalloenzymes is

attempted, and their catalytic abilities are tested.[8] As iron and manganese metals are most commonly found in the active sites of many metalloenzymes and possess potent catalytic abilities, there is a growing interest in studying the structure and reactivity of such species, which is evident from the large body of literature reported in the last decade.[8,10−16]

The study of manganese chemistry is most momentous and has gained much more attention because of its requisite presence in the active site of the water oxidase (WO) enzyme, which performs oxidation of water to dioxygen in the photosynthesis

12085
https://doi.org/10.1021/acs.inorgchem.1c01306
Inorg. Chem. 2021, 60, 12085−12099
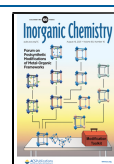
Scheme 1. (a) A Comparative Structure of Me$_2$EBC with the Popular 14-TMC Ligand and (b) the *cis*-Configuration Structures of Mn-Bound Models Studied Here
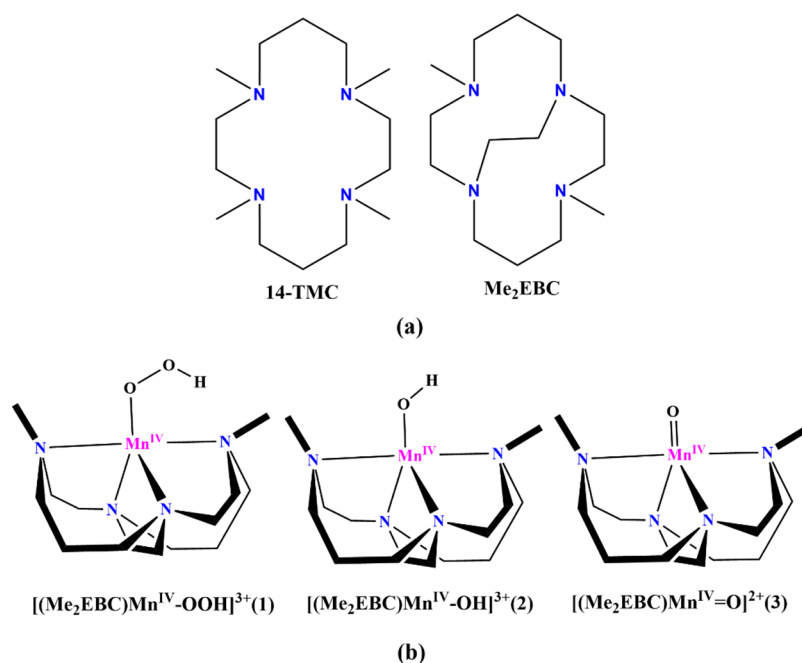
process (photosystem-II, PSII).[1] The OEC (oxygen-evolving complex) resides in an oxo-bridged tetranuclear manganese cluster (Mn$_4$Ca) surrounded by a hydrogen bonding network.[1,17] It is also present in the other enzymes such as Mn-catalase[3] and Mn-superoxide dismutase (MnSOD).[18,19] A growing interest in this study fascinated us to explore these high-valent metal-hydroperoxo species as a possible oxidant in various chemical reactions. Although various important species such as Mn^{III}−OOH, Mn^{IV}−OOH, Mn^{III}=O/Mn^{III}−OH, Mn^{IV}=O/Mn^{IV}−OH, and Mn^V=O have been implicated in reactivity corresponding to various metalloenzymes and their biomimetic models, establishing a comparative oxidative ability of these oxidants for a particular reaction is rare.[20] In this connection, the work of Yin et al. gains attention as they have utilized the [Mn(Me$_2$EBC)Cl$_2$] precursor (here Me$_2$EBC:4,11-dimethyl-1,4,8,11-tetraazabicyclo[6.6.2]hexadecane ligand) to generate various reactive species such as Mn^{IV}−OOH, Mn^{IV}=O, and Mn^{IV}−OH to compare and contrast their oxidative abilities.[21] Their study concludes that Mn^{IV}−OOH is a powerful oxidant compared to the other two species in hydrogen abstraction and oxygenation reactions. It is important to note here that the Me$_2$EBC ligand is similar to the popular 14-TMC ligand and is also called cross-cyclam. The only difference is the presence of ethyl linker connecting two *trans*-nitrogen atoms in the place of terminal methyl group and this link enforces the folding of the macrocycle leading to a *cis*-configuration (see Scheme 1).

To understand the relative oxidative abilities of Mn^{IV}−OOH, Mn^{IV}=O, and Mn^{IV}−OH species, here, we undertake theoretical studies based on density functional and ab initio methods to answer the following intriguing questions: (i) what is the ground state nature of the Mn^{IV}−OOH species, considering electromers such as Mn^{III}−•OOH species? (ii) Is density functional theory (DFT) calculation an unabated tool compared to popular methods such as DLPNO-CCSD(T)? (iii) In the sulfoxidation reaction by Mn^{IV}−OOH species, what are the exact mechanisms, and how large are the kinetic barriers? (iv)

Why Mn^{IV}=O and Mn^{IV}−OH species are unreactive toward oxygen atom transfer (OAT) reaction, whereas other equivalent species perform such transformations at ease? (v) What are the comparative oxidative abilities of these species, and why do they differ in the way they do?

■ COMPUTATIONAL METHODOLOGY

We have performed the calculations using the Gaussian 09 suite of programs and ORCA 4.2.1 program packages.[22−24] The geometries were optimized using the B3LYP-D2 functional, which incorporates the dispersion proposed by Grimme.[25] Two different basis sets were used: LanL2DZ encompasses a double ζ-quality basis set with the Los Alamos effective core potential for Mn[26−28] and a 6-31G* basis set for the other atoms[29] and optimized geometries were then used to perform single-point energy calculations using a TZVP[30,31] basis set on all atoms. Frequency calculations were performed on the optimized structures to verify that they are minima on the potential energy surface (PES) and also to obtain free-energy corrections. The quoted DFT energies are B3LYP-D2 solvation, including free-energy corrections with the TZVP basis set at the temperature of 298.15 K, unless otherwise mentioned. The optimized geometries were verified by animating frequency by using Chemcraft software.[32] The solvation energies were computed at the B3LYP-D2 level using a polarizable continuum model (PCM) with *t*-butanol as a solvent.[33] We have tested the D3 dispersion at B3LYP-D3/TZVP(all atoms)//B3LYP-D3/LanL2DZ(Mn),6-31G*(C, H, N, O) level of theory for selected species and only marginal differences are noted (see Table S8 in ESI). Although the chosen methodology is shown to yield a good numerical estimate of spin-state energetics and thermodynamic/kinetic data,[9,16,34−43] it has been shown in several cases that when two spin states lie very close to each other, the DFT methods fail to predict correct ground state.[44−50] A limited benchmarking was undertaken with BP86, TPSSh, PBE0, M06L, and wB97XD functionals to understand the small energy gap computed, which suggests that the B3LYP method chosen is

reliable if the gap is sufficiently large (see Table S9 in the ESI). The ab initio DLPNO-CCSD(T) has recently gained popularity because of its high accuracy in predicting the correct ground state relative to experimental observations[50,51] and its affordability for larger molecules. Here we have employed DLPNO-CCSD(T) methods to gain insight into the ground state configuration of $Mn^{IV}-OOH$ moiety in comparison to its electromers. We have followed the same protocol as reported in our previous report.[50] The DLPNO-CCSD(T) calculations were performed using the ORCA 4.2.1 program package.[23,24] Here, we have used the optimized structure coordinates from DFT and performed single-point gas-phase DLPNO-CCSD(T) calculations with the Dunning et al. correlation-consistent cc-PVTZ basis set for all atoms and employed TIGHTPNO criteria and the RIJCOSX approximation in our calculations. The state-average complete-active space self-consistent field (SA-CASSCF) calculations were carried out with an active space of three (Mn^{IV}) or four (Mn^{III}) electrons in five 3d-orbital, i.e., CAS(3,5) [10-quartet and 40-doublets] or CAS(4,5) [5-quintets, 45-triplets, and 50-singlets] using the ORCA program. The N-electron valence perturbation theory second order (NEVPT2) incorporates the dynamic correlation in the CASSCF part. Here, the relativistic effects are included via zeroth-order regular approximation (ZORA) with ZORA-contracted basis sets ZORA-def2-TZVP for Mn; ZORA-def2-TZVP(−f) for N, O; and ZORA-def2-SVP for the rest of atoms.[52,53] The Natural Population Analysis (NPA) charges, Wiberg Bond Index (WBI), and Natural Bond Order (NBO) analysis have been performed at the B3LYP-D2/TZVP (all atoms) level of theory using the NBO program (version 3.1) implemented in Gaussian 09.[54,55] The energy decomposition analysis (EDA) was carried out using AOMix software.[56] Herein, we have used notations for all the species such as $^{M}[Symbol]_{sMn,sOOH}$, where superscript "M" denotes the total multiplicities of the species, "Symbol" denotes the species, and the subscript sMn represents the high-spin (hs), intermediate-spin (is), and low-spin (ls) states while up and down radical for sOOH is indicated **u** and **d**, respectively. For example, the representation $^{6}1a_{hs,u}$ indicates the sextet state (Multiplicity, M = 6 for $S = 5/2$) of species **1a**, where Mn is in high-spin (hs) state ($S = 2$) and u indicates the up radical on OOH. Time-dependent density functional theory (TD-DFT) has been performed using the ORCA program with ZORA and RIJCOSX at the B3LYP/def2-TZVP level of theory and the electron paramagnetic resonance (EPR) g-value for $^{4}1a_{hs,d}$ is also computed at the same level.

■ RESULTS

We will begin our discussion with the geometry, electronic structure, and bonding of $[(Me_2EBC)Mn^{IV}-OOH]^{3+}(\mathbf{1})$, $[(Me_2EBC)Mn^{IV}-OH]^{3+}(\mathbf{2})$, and $[(Me_2EBC)Mn^{IV}=O]^{2+}(\mathbf{3})$ species. Experimental studies were carried out at pH = 1.5 (a highly acidic condition). At this experimental condition, water molecule, if any, coordinated to the metal center expect to cleave leaving a five coordinate intermediate as hypothesized here. The second part will expand the discussion to OAT reaction with benzyl phenyl sulfide substrate that reacts the fastest among the substrate tested.[20]

Electronic Structure and Bonding Nature of High-Valent $Mn^{IV}-OOH$ (1), $Mn^{IV}-OH$ (2), and $Mn^{IV}=O$ (3) Species. In all three species, $Mn^{IV}-OOH$ (**1**), $Mn^{IV}-OH$ (**2**), and $Mn^{IV}=O$ (**3**), the coordination environment and oxidation states are similar. We have considered two possible spin states

for Mn^{IV}, i.e., a quartet $S = 3/2$ state corresponding to a high-spin ion and a doublet $S = 1/2$ state corresponding to a low-spin ion.

$[(Me_2EBC)Mn^{IV}-OOH]^{3+}(\mathbf{1})$. For $Mn^{IV}-OOH$, we have considered a possibility that it may exist in one of its electromeric forms, i.e., $Mn^{III}-{}^{\bullet}OOH$. The $Mn^{III}-{}^{\bullet}OOH$ species can have $S = 5/2$ ($S = 3/2$) state, if a ferromagnetic (antiferromagnetic) coupling between high-spin Mn^{III} and ${}^{\bullet}OOH$ is assumed or an $S = 3/2$ ($S = 1/2$) state, if ferromagnetic (antiferromagnetic) coupling, between low-spin Mn^{III} and ${}^{\bullet}OOH$ is assumed. We have computed all possible spin states for $Mn^{IV}-OOH$, and computed energetics are summarized in Table 1. In addition to spin-state divergence, there is also

Table 1. All the Possible Spin Configurations of $Mn^{III}-{}^{\bullet}OOH$ (1a) and $Mn^{IV}-OOH$(1b) with Their Relative DFT Gibbs Free Energies (ΔG) and DLPNO-CCSD(T) Energies (ΔE) in kJ/mol

species	Mn^{III}	${}^{\bullet}OOH$	DFT ΔG (kJ/mol)	DLPNO-CCSD(T) ΔE (kJ/mol)
$^{6}1a_{hs,u}$	↑↑↑↑	↑	10.9	27.7
$^{4}1a_{hs,d}$	↑↑↑↑	↓	0.0	59.7
$^{4}1a_{is,u}$	↑↑↑↓	↑	108.4[a]	
$^{2}1a_{is,d}$	↑↑↑↓	↓	64.5	139.9
$^{2}1a_{ls,u}$	↑↑↓↓	↑	121.7	131.5
	Mn^{IV}	^{-}OOH		
$^{4}1b_{hs}$	↑↑↑		3.4	0.0
$^{2}1b_{ls}$	↑↑↓		118.7	171.0

[a]Single-point energy calculation over the optimized geometry of $^{2}1a_{is,d}$.

structural divergence, i.e., $Mn^{IV}-OOH$ can adopt two distinct structures, $Mn^{III}-\eta^1-{}^{\bullet}OOH$ (**1a**) (side-on) or $Mn^{IV}-\eta^2-OOH$ (**1b**) (end-on), both of which are modeled.

As discussed above, **1a** has five possible electronic configurations, whereas **1b** has only two electronic configurations (see Table 1). The computed energetics for **1a** suggests the quartet spin state $^{4}1a_{hs,d}$ (see computational details for the explanation on the notation) where high-spin Mn^{III} ($S = 2$) antiferromagnetic coupled with hydroperoxyl radical (${}^{\bullet}OOH$) is the ground state. This is followed by $^{6}1a_{hs,u}$, $^{2}1a_{is,d}$, and $^{2}1a_{ls,u}$ species at 10.9, 64.5, and 121.7 kJ/mol, respectively, higher.[57] For **1b**, our calculations reveal that the quartet state $^{4}1b_{hs}$ as a ground state with a doublet state $^{2}1b_{ls}$ is estimated to be 115.3 kJ/mol higher in energy. The energy difference between $^{4}1a_{hs,d}$ and $^{4}1b_{hs}$ is estimated to be 3.2 kJ/mol, and such a small energy difference suggests that these two species are nearly degenerate and easily interconvertible (see Table 1, ΔG values). The DLPNO-CCSD(T) method, on the other hand, predicts that $^{4}1b_{hs}$ as the ground state with other spin-state energies predicts to lie further than the values estimated from DFT methods (see Table 1). The low-spin $S = 1/2$ state of Mn ions is consistently predicted to be very high in energy both in DFT and DLPNO-CCSD(T) methods, suggesting that these states are unlikely to participate in the reaction mechanism.

The computed eigenvalue plot for the ground state of **1a** and **1b** is shown in Figures S1a,b, respectively. The geometry around the Mn ion in **1a** is a distorted square pyramidal geometry, and the $\sigma^*_{z^2}$ orbital is found to lie along the vacant coordination sphere resulting in less repulsion and hence are relatively stabilized compared to the $\sigma^*_{x^2-y^2}$ orbital. As the −OOH group
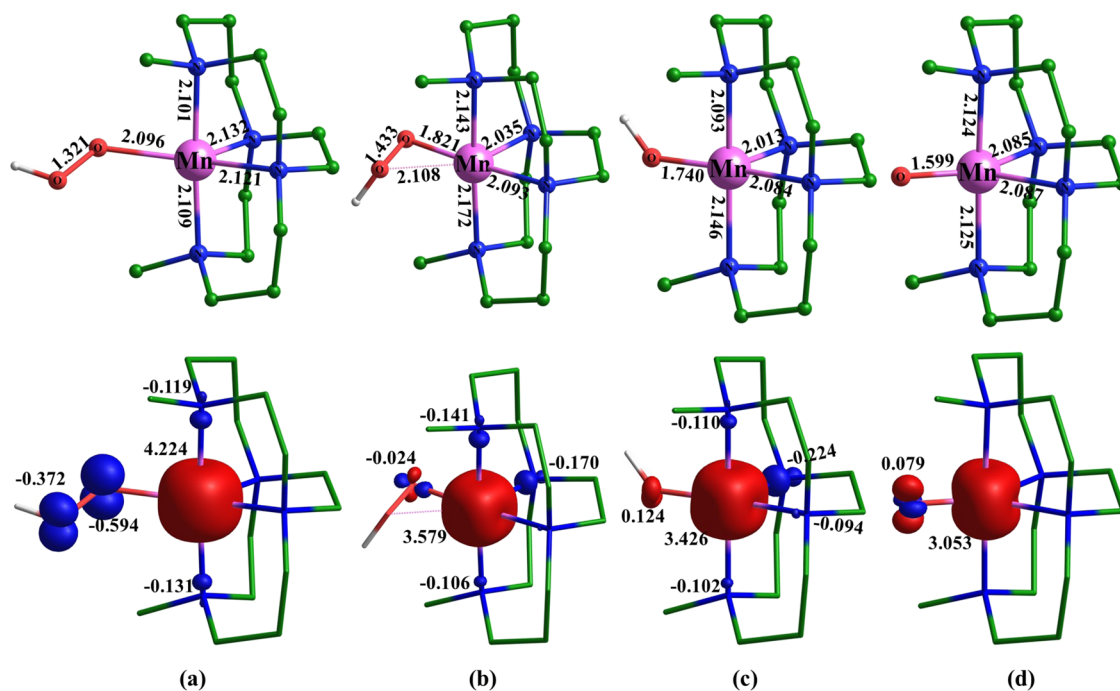
Figure 1. B3LYP-D2 computed optimized structure and its corresponding spin-density plots for species (a) $^4\mathbf{1a_{hs,d}}$, (b) $^4\mathbf{1b_{hs}}$, (c) $^4\mathbf{2}$, and (d) $^4\mathbf{3}$.

lies in the xy plane, the π^*_{yz} orbitals form a weak π-bonding with the hydroperoxy group leaving the d_{xy} and d_{xz} orbitals nonbonding δ_{xy} and δ_{xz}.

The electronic configuration for the ground state ($S = 3/2$) of the species $\mathbf{1a}$ is computed to be $(\delta_{xy})^{\uparrow}(\delta_{xz})^{\uparrow}(\pi^*_{yz})^{\uparrow}(\pi^*_{OOH})^{\downarrow}(\sigma^*_{z^2})^{\uparrow}(\sigma^*_{x^2-y^2})^{0}$ (see Figure S1a). For the $Mn^{IV}-\eta^2-OOH$ species, the ground state electronic configuration is $(\delta_{xz})^{\uparrow}(\pi^*_{xy})^{\uparrow}(\pi^*_{yz})^{\uparrow}(\sigma^*_{z^2})^{0}(\sigma^*_{x^2-y^2})^{0}$ with a stronger π interaction with the d_{yz} and d_{xy} orbitals leaving d_{xz} orbital, as δ_{xz} bonding. For the interconversion of $\mathbf{1a}$ to $\mathbf{1b}$, the $\sigma^*_{z^2}$ α-electron pairs up with the β-electron in π^*_{OOH} orbital leading to a $Mn^{IV}-\eta^2-OOH$ species (see Figure S1a,b). It is an established fact that Mn^{IV} species show a multiconfigurational character.[35,58,59] To understand the multiconfigurational character of true Mn^{IV} species, we have performed state-average CASSCF/NEVPT2 calculations on the $S = 3/2$ ground state of $\mathbf{1b}$. The calculations suggest a strong mixing of ground state configuration ($(\delta_{xz})^{\uparrow}(\pi^*_{xy})^{\uparrow}(\pi^*_{yz})^{\uparrow}(\sigma^*_{z^2})^{0}(\sigma^*_{x^2-y^2})^{0}$ 47.6%) with three excited state quartet configurations ($(\delta_{xz})^{\uparrow}(\pi^*_{xy})^{\uparrow}(\pi^*_{yz})^{0}(\sigma^*_{z^2})^{\uparrow}(\sigma^*_{x^2-y^2})^{0}$ 15.6%, $(\delta_{xz})^{\uparrow}(\pi^*_{xy})^{\uparrow}(\pi^*_{yz})^{0}(\sigma^*_{z^2})^{0}(\sigma^*_{x^2-y^2})^{\uparrow}$ 13.3% and $(\delta_{xz})^{\uparrow}(\pi^*_{xy})^{0}(\pi^*_{yz})^{\uparrow}(\sigma^*_{z^2})^{0}(\sigma^*_{x^2-y^2})^{\uparrow}$ 12.0% see Table S4). Such strong mixing suggests a multiconfigurational character for $\mathbf{1b}$. The NEVPT2 calculations also yield the zero-field splitting (ZFS) parameter as ±0.38 cm^{-1} (D) and 0.33 (E/D), and these are in the range expected for Mn^{IV} species reported in the literature.[60] A small D value obtained here is because of its competing positive and negative contributions to the D arising from the excitation of an electron among d-orbitals with the same or different m_l values. Further isotropic g-tensor calculated for $^4\mathbf{1a_{hs,d}}$ is to be 1.855, which is in excellent agreement with the g-value of 1.854 obtained from the EPR spectrum reported. The TD-DFT calculations have been performed to thoroughly understand the spectral parameters for $^4\mathbf{1a_{hs,d}}$ and $^4\mathbf{1b}$. The TD-DFT spectral features for these two species are very different from each other. The TD-DFT spectrum for $^4\mathbf{1a_{hs}}$ species

shows only three important peaks at 404 nm ($\pi^*_{Me2EBC} \rightarrow \sigma^*_{x^2-y^2}$), 833 nm ($\sigma^*_{z^2} \rightarrow \sigma^*_{x^2-y^2}$), and 1263 nm ($\sigma^*_{z^2} \rightarrow \pi^*_{OOH}$), whereas $^4\mathbf{1b}$ species spectrum shows several features starting at 276 nm ($\pi^*_L \rightarrow \sigma^*_{x^2-y^2}$), 320 nm ($\pi^*_L \rightarrow \pi^*_{xy}$), 362 nm ($\pi^*_L \rightarrow \sigma^*_{x^2-y^2}$), 396 nm ($\pi^*_L \rightarrow \sigma^*_{z^2}$), 484 nm ($\pi^*_{Mn(dxy)-L} \rightarrow \sigma^*_{z^2}$), 546 nm ($\pi^*_L \rightarrow \sigma^*_{z^2}$), and 642 nm ($\pi^*_L \rightarrow \sigma^*_{z^2}$) (see Figure S14a,b in ESI). The $Mn^{III}-{}^{\bullet}OOH$ exhibits less ligand to metal charge transfer (LMCT) transitions, whereas $Mn^{IV}-OOH$ exhibits many LMCT transitions, and this observation is in excellent agreement with previous reports, offering confidence in the computed data/mechanism.[61]

The optimized structure and spin-density plots of the ground spin states of species $\mathbf{1a}$ and $\mathbf{1b}$ are shown in Figure 1a,b. The Mn–O (O–O) bond length is 2.096 (1.321) Å for $^4\mathbf{1a_{hs,d}}$ and 1.821 (1.433) Å for $^4\mathbf{1b_{hs}}$, revealing variation in the oxidation state as indicated. The shorter O–O distance found for $\mathbf{1a}$ is consistent with the hydroperoxy radical species (see Table S1-S3). The spin density on the Mn and OOH groups of $^4\mathbf{1a_{hs,d}}$ is found to be 4.224 and -0.966, respectively, which indicates an antiferromagnetic interaction between Mn and OOH moieties (see Table S1-S3). In the $^4\mathbf{1b_{hs}}$, the spin densities on Mn and OOH are 3.579 and -0.024, respectively (see Figure 1b). NBO analysis indicates that the Mn–O bond is ionic with 77.14% Mn-(d_{z^2}) (74.12%) contribution and 22.86% (25.88%) from O1(p_z) orbital for $^4\mathbf{1a_{hs,d}}$ ($^4\mathbf{1b_{hs}}$). The WBI for Mn–O1 bond in $^4\mathbf{1a_{hs,d}}$ is 0.343, which suggests that this bond is a weak single bond while WBI for Mn–O1 and Mn–O2 bonds in $^4\mathbf{1b_{hs}}$ is found to be 0.742 and 0.335, respectively, which indicates the η^2-type bonding of −OOH moiety (see Figure S2).

$[(Me_2EBC)Mn^{IV}-OH]^{3+}$ (2). We have optimized all the possible spin states of $[(Me_2EBC)Mn^{IV}-OH]^{3+}$(2). We have also attempted to compute the electromeric form of $Mn^{IV}-OH$., i.e., $Mn^{III}-{}^{\bullet}OH$ but this has generated the radical at the nitrogen atom of the Me_2EBC instead of the expected oxygen atom whose energy is also very high (see Table S10 in ESI). Furthermore, a coordinate scan performed by varying the Mn–OH distance also yielded radical electromeric species, which are very high in

Scheme 2. Proposed Mechanism for the OAT Reaction of Benzyl Phenyl sulfide (S) Leading to the Formation of Oxidized Product Benzyl Phenyl Sulfoxide (P) by an Attack on the (a) Distal Oxygen (O(2), Pathway *a*) and (b) Proximal Oxygen (O(1), Pathway *b*) of [(Me$_2$EBC)Mn^{IV}−OOH]$^{3+}$ (1)

(a)

(b)
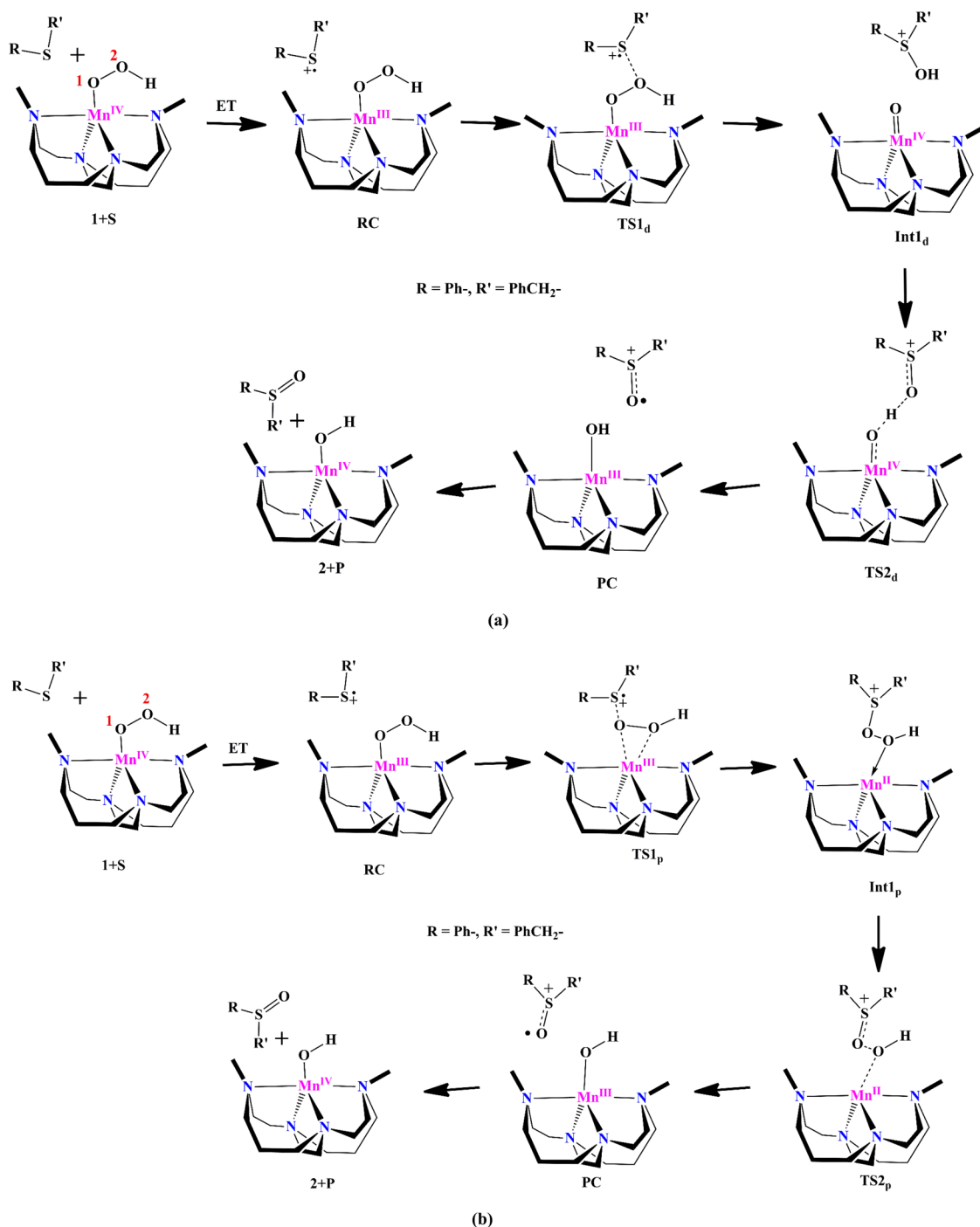
energy compared to the ground state structure. These additional calculations suggest that such electromeric forms are unlikely for the hydroxy counterparts (see Figure S12 in ESI).

Our calculations suggest that the quartet state ^{4}2 is the ground state, with doublet state ^{2}2 lying higher at 111.0 kJ/mol. This gap is much higher than that observed in [(Me$_2$EBC)Mn^{IV}−OOH]$^{3+}$(1a) species. The optimized structure and spin-density plot of Mn^{IV}−OH are given in Figure 1c. The Mn−OH bond distance for ^{4}2 is found to be 1.740 Å, which is shorter than that of ^{4}1a$_{hs,d}$ (2.096 Å) and ^{4}1b$_{hs}$ (1.821 Å), and this distance is also within the range of Mn−O single bond. The spin-density plot of

^{4}2 suggests that the spin polarization from the Me$_2$EBC ligand nitrogen and delocalization from oxygen leads to the 3.426 spin density on Mn metal. Further NBO analysis reveals that Mn−O σ-bond is more ionic in ^{4}2 than in ^{4}1b$_{hs}$. For ^{4}2, the Mn−O σ-bonding interaction is composed of 19.34% of Mn (d$_z^2$) and 80.66% of O (p$_z$) orbitals (see Figure S3). The WBI is estimated to be 0.906, revealing only a single σ-bond between the Mn and oxygen atoms. The WBI for the Mn−O bond in ^{4}1b$_{hs}$ is lower than that of ^{4}2, which suggests that the Mn−O bond is stronger in the case of ^{4}2 compared to ^{4}1b$_{hs}$.
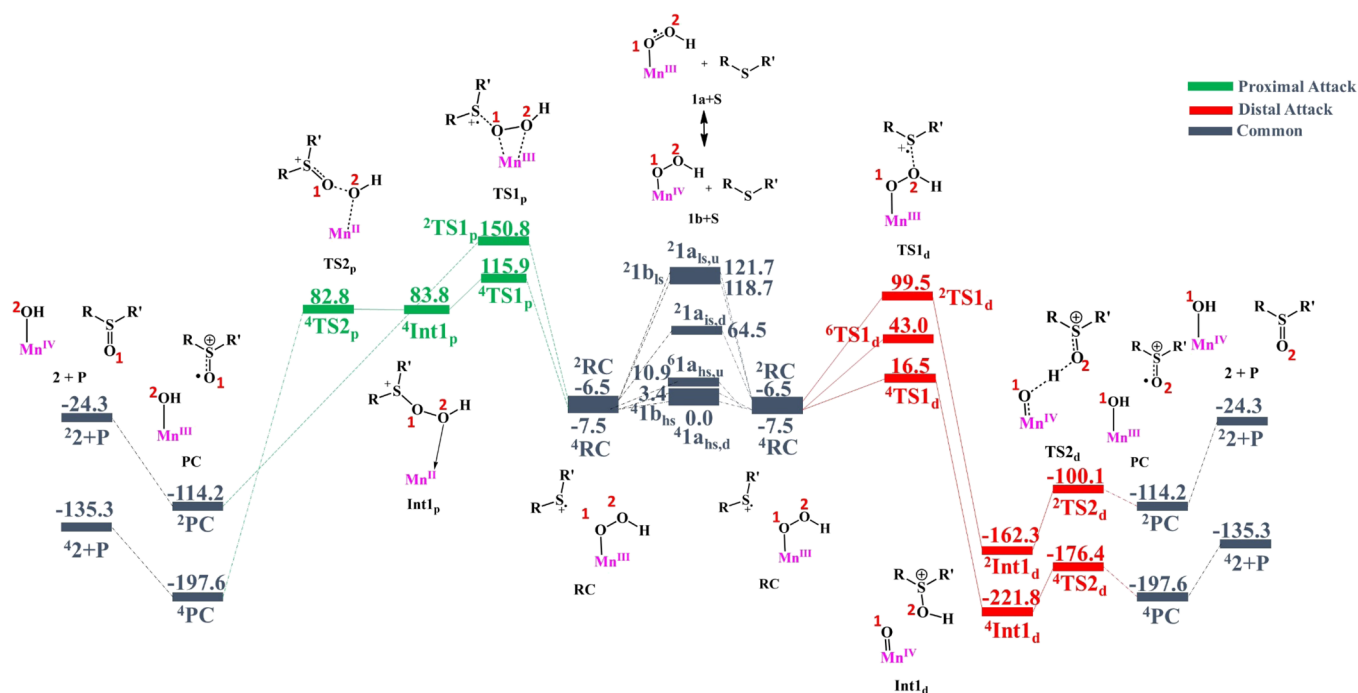
Figure 2. B3LYP-D2 computed PES (ΔG in kJ/mol) for the OAT reaction of benzyl phenyl sulfide (**S**), leading to the formation of oxidized product benzyl phenyl sulfoxide (**P**) by the attack on the distal oxygen (O(2), pathway a, red color) and proximal oxygen (O(1), pathway b, green color) of $[(Me_2EBC)Mn^{IV}-OOH]^{3+}$ (**1**). For clarity, the Me$_2$EBC ligand is not shown. The ΔG for RC and PC is derived from IRC plots (see the Supporting Information).

The geometry around the Mn ion in Mn^{IV}−OH species is a distorted square pyramidal geometry, leading to the stabilization of $\sigma*_{z^2}$ orbital compared to the $\sigma*_{x^2-y^2}$ orbital. The electronic configuration for the ground state ($S = 3/2$) of the species Mn^{IV}−OH is computed to be $(\delta_{xz})^{\uparrow}(\pi*_{yz})^{\uparrow}(\pi*_{xy})^{\uparrow}(\sigma*_{z^2})^0(\sigma*_{x^2-y^2})^0$ (see Figure S1c). The CASSCF/NEVPT2 calculations for **2** also reveal a multi-configurational character with 30.5% for the ground state configuration $(\delta_{xz})^{\uparrow}(\pi*_{yz})^{\uparrow}(\pi*_{xy})^{\uparrow}(\sigma*_{z^2})^0(\sigma*_{x^2-y^2})^0$, which is mixed with the three excited $S = 3/2$ states $(\delta_{xz})^{\uparrow}(\pi*_{yz})^{\uparrow}(\pi*_{xy})^0(\sigma*_{z^2})^{\uparrow}(\sigma*_{x^2-y^2})^0$, $(\delta_{xz})^{\uparrow}(\pi*_{yz})^{\uparrow}(\pi*_{xy})^0(\sigma*_{z^2})^0(\sigma*_{x^2-y^2})^{\uparrow}$, and $(\delta_{xz})^{\uparrow}(\pi*_{yz})^0(\pi*_{xy})^{\uparrow}(\sigma*_{z^2})^0(\sigma*_{x^2-y^2})^{\uparrow}$ by 28.4%, 16.7%, and 11.2% contributions, respectively (see Table S4). The computed D and E/D values for this species are 1.31 cm^{-1} and 0.11, respectively (see Table S4). These D values are relatively small because of a mixture of positive and negative contributions due to excitation among the same/different m_l level d-orbitals. The TD-DFT spectrum for ^{4}**2** also shows seven peaks nearly same as ^{4}**1b**$_{hs}$ at 300 nm ($\pi*_{Mn(dxy)-L} \rightarrow \sigma*_{x^2-y^2}$), 346 nm ($\pi*_L \rightarrow \pi*_{xy}$), 380 nm ($\pi*_{xz} \rightarrow \sigma*_{x^2-y^2}$), 410 nm ($\pi*_L \rightarrow \sigma*_{x^2-y^2}$), 543 nm ($\pi*_{Mn(dxy)-L} \rightarrow \sigma*_{z^2}$), 631 nm ($\pi*_{xz} \rightarrow \sigma*_{z^2}$), and 750 nm ($\pi*_L \rightarrow \sigma*_{z^2}$) (see Figure S14c in ESI). Like Mn^{IV}−OOH, Mn^{IV}−OH also shows a larger number of LMCT transitions, which agrees with previous experimental reports.[61]

*[(Me$_2$EBC)Mn^{IV}=O]$^{2+}$(**3**).* The well-known high-valent Mn^{IV}=O species $[(Me_2EBC)Mn^{IV}=O]^{2+}$(**3**) has been studied to understand its role during the OAT reaction. The optimization of all the possible spin states in this case also suggests that the quartet spin state (^{4}**3**) is the ground state with respect to a doublet spin state (^{2}**3**), which is 59.5 kJ/mol higher in energy. In addition to these spin states, we have also considered electromeric Mn^{III}−O$^{\bullet}$ of Mn^{IV}=O. This species is calculated to be higher in energy than in the ground state ($S = 5/$

2 at 41.5 kJ/mol and $S = 3/2$ at 23.4 kJ/mol) and unlikely to participate in the reaction mechanism (see Table S10). The optimized structure and its corresponding spin-density plot of ^{4}**3** are shown in Figure 1d. The Mn−O bond length for ^{4}**3** is 1.599 Å which agrees with the previously reported Mn−O bond length in high-valent Mn^{IV}=O species.[16,35−37] The spin density on the Mn atom of ^{4}**3** is 3.053, suggesting moderate spin-polarization as the spin density is slightly larger than the expected value for three unpaired electrons. The NBO analysis of ^{4}**3** indicates one σ bond and one π bond, i.e., Mn=O (see Figure S4). The Mn−O σ-bonding interaction is composed of 21.07% of Mn(d$_{z^2}$) and 78.93% of O(p$_z$) orbitals, and this suggests an ionic character for this bond. The Mn−O π-bonding interaction is composed of d$_{xz}$-p$_x$ with 35.62 and 64.38% from Mn and O orbitals, respectively (see Figure S4).

Unlike **1** and **2**, the geometry around the Mn ion in Mn^{IV}=O species is a distorted trigonal bipyramidal geometry instead of a distorted square pyramidal geometry. The electronic configuration for the ground state ($S = 3/2$) of the species Mn^{IV}=O is computed to be $(\delta_{xz})^{\uparrow}(\delta_{x^2-y^2})^{\uparrow}(\pi*_{yz})^{\uparrow}(\pi*_{xy})^0(\sigma*_{z^2})^0$ (see Figure S1d). The CASSCF/NEVPT2 calculations for Mn^{IV}=O species suggest 66.3% contribution from the ground state with 23.2% contribution from an excited state $(\delta_{xz})^{\uparrow}(\delta_{x^2-y^2})^0(\pi*_{yz})^{\uparrow}(\pi*_{xy})^{\uparrow}(\sigma*_{z^2})^0$ (see Table S4). The computed D and E/D values for this species are 5.60 cm^{-1} and 0.15, respectively (see Table S4), and the D value estimated here is slightly larger than Mn^{IV}−OOH and Mn^{IV}−OH, but the sign of D remains the same as the dominant contributions to the D arise from the same m_l level transition.[38] The TD-DFT spectrum for ^{4}**3** shows five peaks at 275 nm ($\pi*_L \rightarrow \sigma*_{z^2}$), 296 nm ($\pi_{yz} \rightarrow \pi*_{yz}$), 405 nm ($\pi*_L \rightarrow \pi*_{xy}$), 544 nm ($\pi*_{yz} \rightarrow \sigma*_{z^2}$), and 694 nm ($\delta*_{x^2-y^2} \rightarrow \pi*_{xy}$) (see Figure S14d in ESI), with last two transitions are d-d, and the others are LMCT in character.
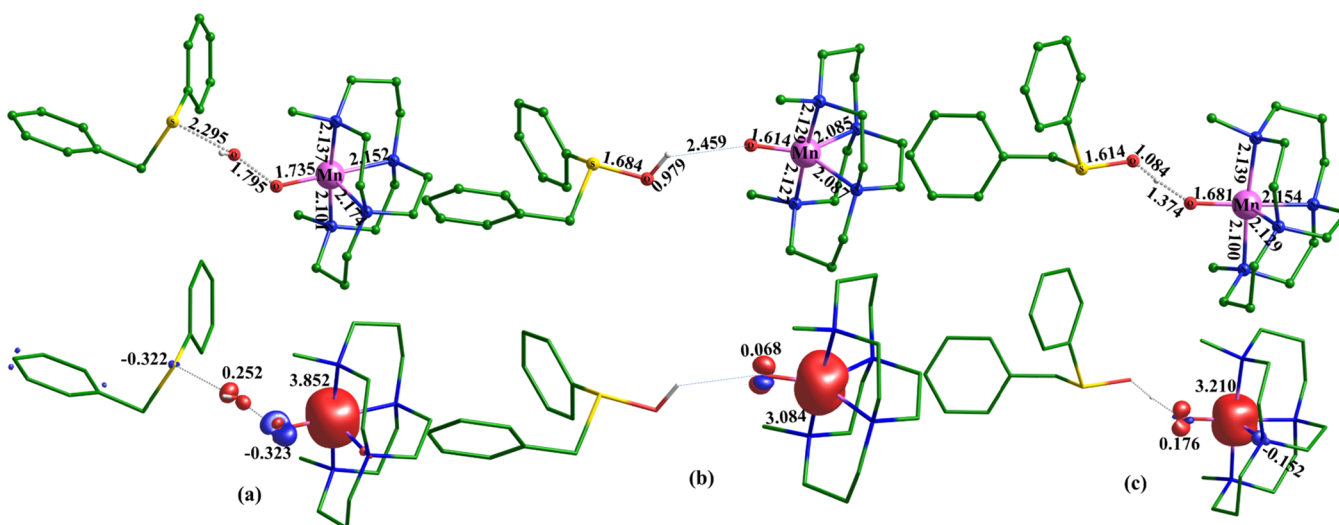
Figure 3. B3LYP-D2 computed optimized transition state and intermediate structures with their corresponding spin-density plots (a) $^4\text{TS1}_d$, (b) $^4\text{Int1}_d$, and (c) $^4\text{TS2}_d$ for the distal attack.

Oxygen Atom Transfer Reaction by Mn^{IV}−OOH. Experimentally, $[(Me_2EBC)Mn^{IV}$−OOH$]^{3+}$ species is found to oxygenate various substrates such as diphenyl sulfide, methyl phenyl sulfide, and benzyl phenyl sulfide with turn-over frequency of 13.8, 15.4, and 17.8 h^{-1}, respectively, at the pH level of 1.5 at a slightly elevated temperature (50 °C). Isotopic labeling experiments confirm that the oxygen atom from the hydroperoxo group is transferred to the substrate. Further control experiments prove that $[(Me_2EBC)Mn^{IV}(OH)_2]^{3+}$ as well as species Mn^{IV}−OH and Mn^{IV}=O are unreactive toward OAT reactions.

To understand the reactivities of these species, we have chosen the most reactive substrate, benzyl phenyl sulfide (**S**), and tested its reactivity toward the OAT to form benzyl phenyl sulfoxide (**P**). Our analysis and detailed intrinsic reaction coordinate (IRC) analysis suggest that the first step of the reaction involves the formation of the reactant complex (**RC**), as depicted in Scheme 2. Analysis of the electronic structure of the **RC** reveals that it had undergone one-electron reduction to $[(Me_2EBC)Mn^{III}$−OOH$]^{2+}$. At the same time, the substrate is oxidized to $[PhCH_2SPh]^{+\bullet}$ species and the **RC** is exothermic from the reactant by 7.5 kJ/mol. The nature of the species is confirmed from the electronic structure and spin-density analysis (see Figure S5). From the **RC**, there are two plausible pathways for the OAT reaction. Among these two pathways, the first pathway (see pathway a, Scheme 2) involves the direct attack to distal oxygen (O(2)) by the sulfur atom of benzyl phenyl sulfide (**S**) to form an intermediate Int1_d through the transition state TS1_d. This intermediate abstracts the hydrogen from the sulfur hydroxyl group through hydrogen atom transfer (HAT) transition state TS2_d to form the product sulfoxide and $[(Me_2EBC)Mn^{IV}$−OH$]^{3+}(\mathbf{2})$ species. Similarly, the attack to the proximal oxygen (O(1)) by the sulfur atom of benzyl phenyl sulfide (**S**) through the TS1_p forms an intermediate Int1_p. The O−O bond cleavage from the Int1_p leads to the formation of benzyl phenyl sulfoxide (**P**) and $[(Me_2EBC)Mn^{IV}$−OH$]^{3+}(\mathbf{2})$ (see pathway b, Scheme 2).

Distal Attack (Pathway a). The distal oxygen of $[(Me_2EBC)Mn^{IV}$−OOH$]^{3+}$ (**1**) attacks via the transition state TS1_d. Among all the three transition states, $^6\text{TS1}_d$, $^4\text{TS1}_d$, and $^2\text{TS1}_d$, the lower energy transition state is $^4\text{TS1}_d$, which has a barrier height of

16.5 kJ/mol with respect to the reactant, whereas the other two transition states are 43.0 kJ/mol ($^6\text{TS1}_d$) and 99.5 kJ/mol ($^2\text{TS1}_d$), which is higher in energy (see Figure 2). The optimized structure and spin-density plot of $^4\text{TS1}_d$ are shown in Figure 3a. The imaginary frequency corresponding to the S...OH bond formation and Mn−O...OH bond cleavage is $i530$ cm^{-1} for $^4\text{TS1}_d$. The bond length of the Mn−O bond decreases from 2.096 Å ($^4\text{1a}_{hs,\,d}$) to 1.735 Å, whereas the O−O bond length increases from 1.321 Å ($^4\text{1a}_{hs,\,d}$) to 1.795 Å, which clearly suggests that the O...O bond is cleaved, and the S...OH bond is formed with a distance of 2.295 Å (see Figure 3a and Table S1). The spin-density plot of $^4\text{TS1}_d$ suggests that the spin-density on the Mn ion at the transition state decreases from 4.224 to 3.852 compared to the reactant. The sulfur atom and −OH group have a spin density of −0.322 and 0.252, respectively.

The transition state TS1_d leads to the formation of intermediate Int1_d. Here, we have found a quartet spin state as the ground state ($^4\text{Int1}_d$) with a doublet spin state ($^2\text{Int1}_d$) lying at 59.5 kJ/mol higher. We have observed that the Int1_d is equivalent to the Mn^{IV}=O (**3**) species as the transfer of −OH to benzyl phenyl sulfide leads to the formation of cationic species $[PhCH_2S(OH)Ph]^+$. A careful observation of the structure and spin-density values $^4\text{Int1}_d$ and $^4\mathbf{3}$ reveals that the $^4\text{Int1}_d$ and $^4\mathbf{3}$ species are similar. The $[PhCH_2S(OH)Ph]^+$ species is attached through a weak hydrogen bonding interaction (O−H bond length = 2.459 Å) to $^4\mathbf{3}$, leading to $^4\text{Int1}_d$. This hydrogen bonding interaction with the substrate leads to a larger Mn−O bond in the $^4\text{Int1}_d$ than $^4\mathbf{3}$ (1.614 vs 1.599 Å) with a smaller change in the spin-density values (Mn = 3.084 vs 3.053, see Figures 1d and 3b). The formation of $^4\text{Int1}_d$ is highly exothermic with −221.8 kJ/mol energy.

Finally, benzyl phenyl sulfoxide product formation takes place through the HAT transition state TS2_d. A quartet spin state $^4\text{TS2}_d$ is the lowest in energy transition state with an estimated barrier height of 45.4 kJ/mol with respect to the $^4\text{Int1}_d$. However, this is expected to be barrierless from the reactant energy. The $^2\text{TS2}_d$ species is higher in energy by 121.7 kJmol from $^4\text{Int1}_d$, suggesting that the reaction takes place solely in the quartet surface as observed earlier in several Mn^{IV}=O/Mn^{III}=O chemistries.[16,35−37,58−60] The (S)O−H bond length is found to elongate from 0.979 to 1.084 Å at the transition, whereas the
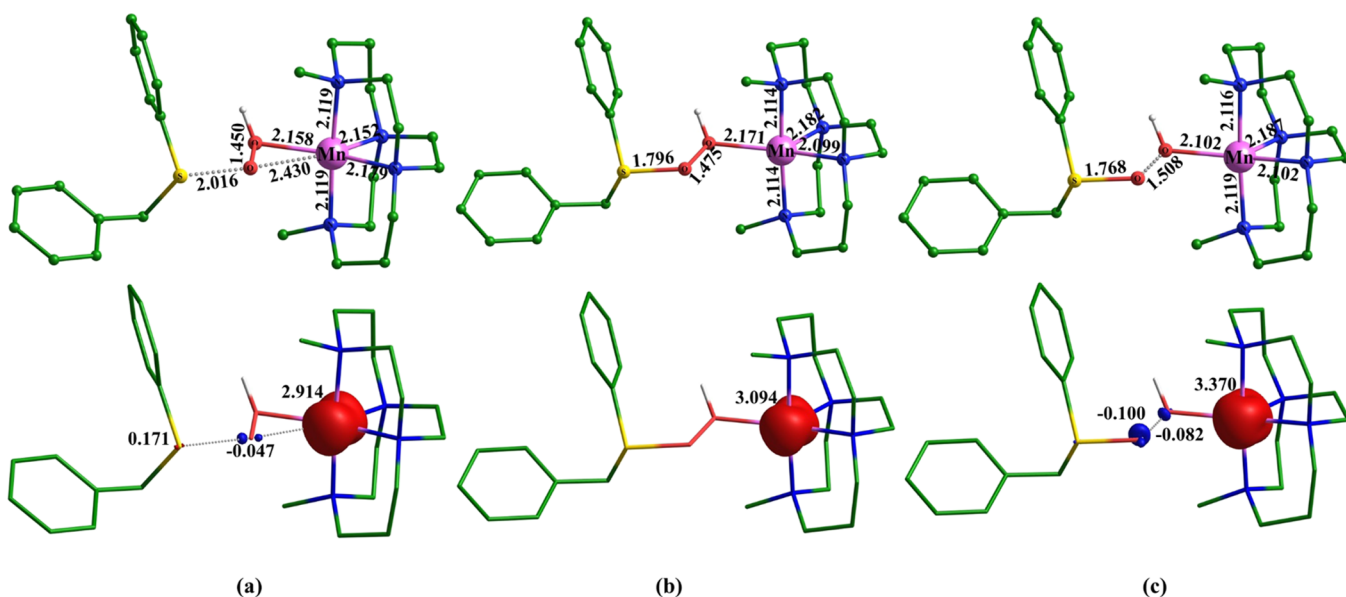
Figure 4. B3LYP-D2 computed optimized transition state and intermediate structures with their corresponding spin-density plots (a) ^{4}TS1$_p$, (b) ^{4}Int1$_p$, and (c) ^{4}TS2$_p$ for proximal attack.

Scheme 3. Proposed Mechanism for the Direct OAT Reaction of Benzyl Phenyl Sulfide (S) Leading to the Formation of the Oxidized Product by (a) $[(Me_2EBC)Mn^{IV}-OH]^{3+}$ (2) and (b) $[(Me_2EBC)Mn^{IV}=O]^{2+}$ (3)
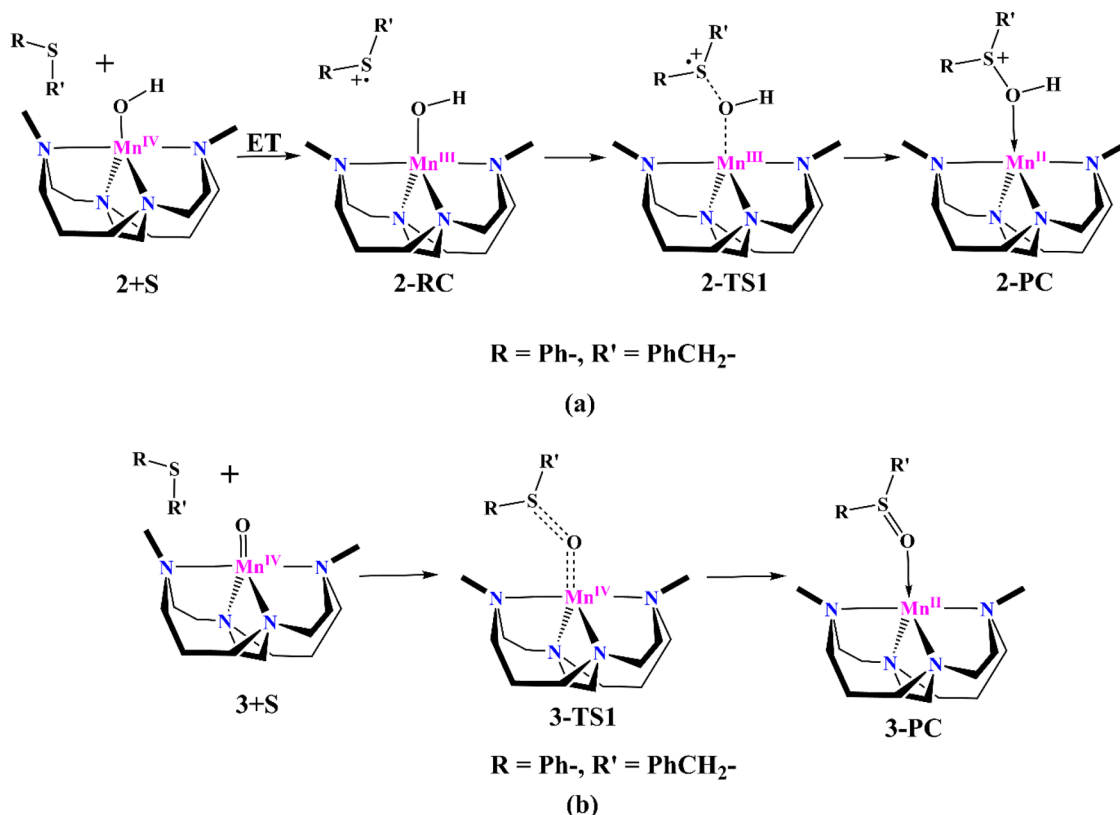
(Mn)O−H bond shrinks from 2.459 to 1.374 Å at the transition state. Also, the S−O bond length decreases from 1.684 to 1.614 Å, whereas the Mn−O bond length increases from 1.614 to 1.681 Å from the intermediate ^{4}Int1$_d$ to the transition state ^{4}TS2$_d$. All these suggest a partial HAT at the transition state (see Figure 3c). The Mn spin-density value increases from 3.084 to 3.210 because of the spin polarization from the attached ligand (see Figure 3b,c).

The IRC plots for ^{4}TS2$_d$ (see Figure S6) reveal that the (S)O−H bond cleaves homolytically leading to the formation of cation radical product $\{[(Me_2EBC)Mn^{III}-OH]^{2+}+[PhCH_2S-(=O)Ph]^{\bullet+}\}$ (PC). The energetics of PC$_d$ was estimated using the IRC structure and ^{4}PC was found to be slightly endothermic with respect to ^{4}Int1$_d$ (24.2 kJ/mol). A similar behavior is also noted for the doublet surface.[62]

At the final step, a one-electron transfer from $[(Me_2EBC)-Mn^{III}-OH]^{2+}$ to $[PhCH_2S(=O)Ph]^{\bullet+}$ leads to the formation of oxidized product benzyl phenyl sulfoxide (**P**) and $[(Me_2EBC)-Mn^{IV}-OH]^{3+}$ (**2**) species. From the product complex, this is found to be endothermic by 62.3 kJ/mol (86.5 kJ/mol from the intermediate $^4Int1_d$) and is exothermic by −135.3 kJ/mol with respect to the reactant.

Proximal Attack (Pathway b). The proximal oxygen of $[(Me_2EBC)Mn^{IV}-OOH]^{3+}$ (**1**) (oxygen attached to Mn) attacks the sulfur through the transition state $TS1_p$. This is preceded by the formation of the **RC**, as mentioned earlier. Here, we have observed that the proximal attack mainly proceeds through $Mn^{III}-OOH$, and so considering this, there are only two transition states possible: quartet ($^4TS1_p$) and doublet ($^2TS1_p$) (multiplicity here is the combined multiplicity of the metal center and the radical cation of the substrate in **RC** with the radical spin-down is assumed). The lowest barrier height for the proximal oxygen attack is 115.9 kJ/mol ($^4TS1_p$) with respect to the reactant, whereas $^2TS1_p$ has a barrier of 150.8 kJ/mol, and the lowest barrier height here is 99.4 kJ/mol higher than pathway *a* (see Figure 2).

Both the Mn−O and Mn−OH bond lengths increase from 1.821 to 2.430 Å and 2.108 to 2.158 Å, respectively, if we move from $^4 1b_{hs}$ to $^4TS1_p$ species. The O−O bond marginally alters during this transition state (see Figures 1b and 4a). Through the spin-density plots of $^4 1b_{hs}$ and $^4TS1_p$, we have found that the spin-density on the Mn atom decreases from 3.579 to 2.914, but this decrease is due to the reduction in the spin polarization from the attached Me_2EBC ligand (see Figure 4a). The transition state $TS1_p$ leads to the intermediate $Int1_p$ where O−O bond is intact. This intermediate is endothermic by 83.8 kJ/mol ($^4Int1_p$) with respect to the reactant. The Mn−OH and O−O bond lengths in the $^4Int1_p$ species are 2.171 and 1.475 Å, respectively (see Figure 4b). The S−O bond length decreases from 2.016 to 1.796 Å, which suggests the formation of a single bond between the sulfur and oxygen atoms in $^4Int1_p$ species. The eigenvalue plot and the spin densities suggest that the Mn atom is in a + 2 oxidation state (see Figure S7). The O−O bond cleavage in the intermediate $Int1_p$ via transition state $TS2_p$ is expected in the next step. This transition state is barrierless as both the energies of $^4Int1_p$ and $^4TS2_p$ are nearly the same (83.8 kJ/mol for $^4Int1_p$ and 82.8 kJ/mol for $^4TS2_p$). The imaginary frequency corresponding to this transition is found to be $i286$ cm^{-1} which corresponds to O−O bond cleavage and S=O double bond formation as the S=O bond distance decreases from 1.796 to 1.768 Å (see Figure 4c). After this transition state, the formation of sulfoxide product (**P**) and $[(Me_2EBC)Mn^{IV}-OH]^{3+}$ (**2**) is expected, and this is found to be exothermic by −197.56 kJ/mol on the quartet surface from the reactant as this step is the same for both pathways *a* and *b*.

Oxygen Atom Transfer Reaction by Mn^{IV}−OH and Mn^{IV}=O. To understand the reactivity difference between $[(Me_2EBC)Mn^{IV}-OOH]^{3+}$ (**1**) and $[(Me_2EBC)Mn^{IV}-OH]^{3+}$ (**2**) and $[(Me_2EBC)Mn^{IV}=O]^{2+}$ (**3**), we have computed the direct OAT using Mn^{IV}−OH and Mn^{IV}=O species with benzyl phenyl sulfide as substrate (**S**) (see Scheme 3). In the first step, the formation of the **RC** occurs, and its formation is exothermic for **2** (−72.4 kJ/mol). For species **3**, the **RC** formation is endothermic and suggests that such species unlikely exists for **3**. The OAT transfer reaction for both the species proceeds via **TS1** (see Scheme 3a,b), and for **2**, the barrier height is estimated to be 137.7 kJ/mol from ^{4}**2-RC** (65.3 kJ/mol from **2**) for the quartet transition ^{4}**2-TS1** and the doublet transition

state (^{2}**2-TS1**) lying at 123.9 kJ/mol from **2** (see Figure 5a). The product formation is exothermic from the separate reactant but
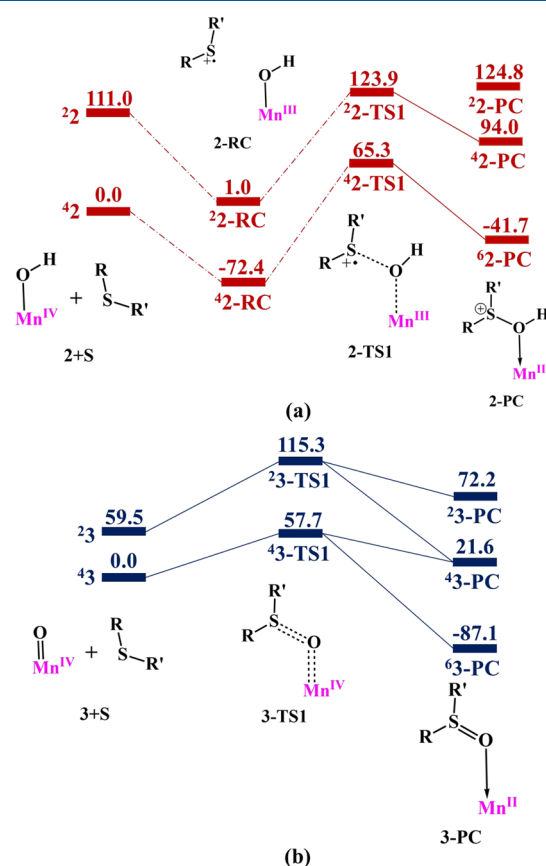
Figure 5. B3LYP-D2 computed PES (ΔG in kJ/mol) for the OAT from (a) $[(Me_2EBC)Mn^{IV}-OH]^{3+}$ (**2**) and (b) $[(Me_2EBC)Mn^{IV}=O]^{2+}$ (**3**). The ΔG for 2-RC is derived from the IRC plot (see the Supporting Information).

is endothermic from the **RC**. For product, our calculations reveal sextet ^{6}**2-PC** as the ground state (−41.7 kJ/mol from ^{4}**2**), whereas other spin states are found to be higher in energy.

In the case of **3**, the barrier height is computed to be 57.7 kJ/mol for the quartet state (^{4}**3-TS1**) with doublet at 115.3 kJ/mol energy (^{2}**3-TS1**) (see Figure 5b). The imaginary frequency corresponding to this transition is $i601$ cm^{-1}, which indicates the direct transfer of oxygen from **3** to **S**. The Mn−O and S−O bond lengths in the optimized structure of ^{4}**3-TS1** (^{4}**3-PC**) are 1.754 Å (1.991 Å) and 1.925 Å (1.579 Å), respectively (see Table S1 and Figure 6). The significant decrease in the S−O bond length indicates the formation of the S=O double bond, and the Mn ion interacts weakly with oxygen. The formation of the product is exothermic by −87.1 kJ/mol (^{6}**3-PC**) from the reactant and the other two spin states of the product lie much higher in energy (see Table S1 and Figure 6).

■ DISCUSSION

Our DFT as well as DLPNO-CCSD(T) calculations affirm that all the species Mn^{IV}−OOH (**1a**, **1b**), Mn^{IV}−OH (**2**), and Mn^{IV}=O (**3**) have a high-spin ($S = 3/2$) ground state. Except for **1a**, where one β electron is located on the −OOH moiety, the other species **1b**, **2**, and **3** have a small spin density on the oxygen atom (−0.024(**1b**), 0.124(**2**), and 0.079(**3**)). DFT calculations predict a very small energy gap between **1a** and **1b** at
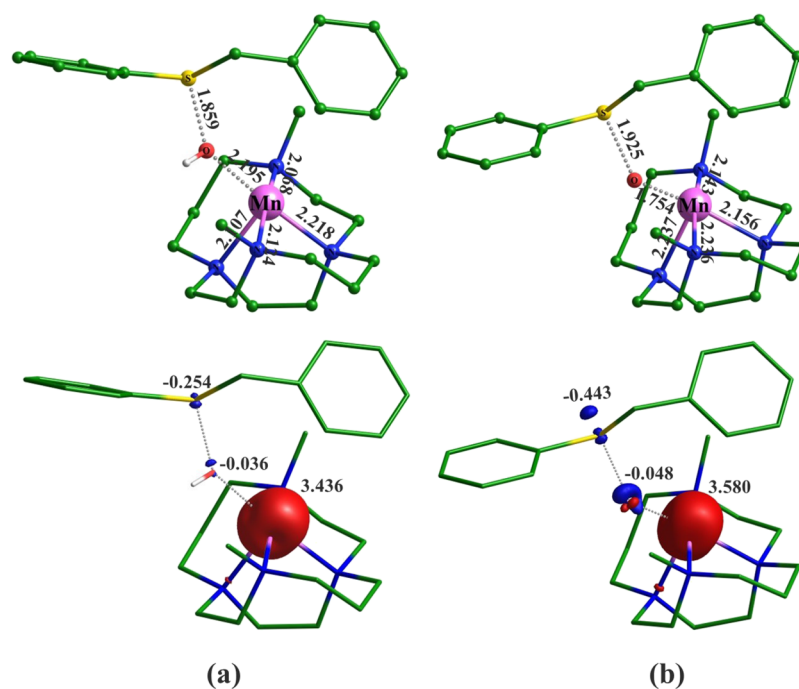
Figure 6. B3LYP-D2 computed optimized transition state structure and its corresponding spin-density plot for (a) ^{4}2-TS1 and (b) ^{4}3-TS1.
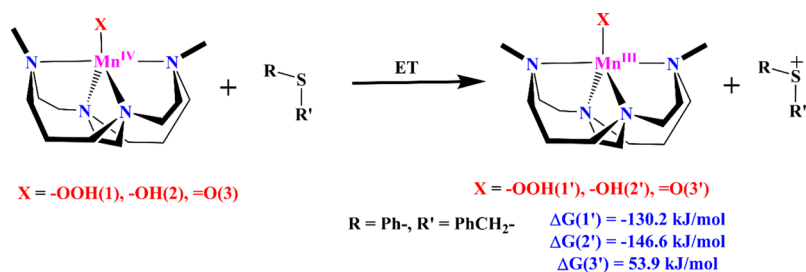
Figure 7. Thermodynamics of ET process of **1**, **2**, and **3** species.

$S = 3/2$ surface, and for these geometries, DLPNO-CCSD(T)−computed gap is much larger, suggesting the importance of such tools in quantifying energy gaps that are too small to predict using conventional DFT methods confidently.[50]

The energy difference between the ground state ($S = 3/2$) and the excited state ($S = 1/2$) for these species is 171.0 kJ/mol (**1b**), 111.0 kJ/mol (**2**), and 59.5 kJ/mol (**3**), and this suggests a possible single-state reactivity for **1b** and **2** while a possible two-state reactivity (TSR) for **3** via low-lying $S = 1/2$ state. For species **1a**, on the other hand, there are two spin states (a sextet and a quartet state which are related to the exchange coupling between the Mn(III) and radical center located at the hydroperoxo units) that are close-lying in energy (10.9 kJ/mol) and offers a possible TSR scenario. Further state-average CASSCF calculations reveal the multiconfigurational character of the ground state in **1b**, **2**, and **3**. The species **1b** (**2**) shows a strong multireference character with 15.6% (28.4%), 13.3% (16.7%), and 12.0% (11.2%) contributions arising from mixing of various $S = 3/2$ states. These states arise due to the mixing of $\sigma^*_{z^2}$ and $\sigma^*_{x^2-y^2}$ orbitals in both cases (see Table S4). Species **3** has a dominant single-reference character compared to the other two species and contributes to its sluggish reactivity.[63] Calculated ZFS parameters for **1b** (**2**) [**3**] were $D = 0.38$ cm^{-1} (1.31 cm^{-1}) [5.60 cm^{-1}] and $E/D = 0.33$ (0.11) [0.15]. Although experimental D and E are not available for Mn^{IV}−

OOH species, recorded X-band EPR reveals sharp features with Mn-hyperfine centered around $g \sim 1.85$, and this suggests that the D value is likely to be very small, and this is consistent with the computed values. The computed g-tensor for the ground state of **1a**, i.e., ^{4}**1a**$_{hs,d}$ is in excellent agreement with experiments. The computed TD-DFT spectra for Mn^{III}−$^\bullet$OOH and Mn^{IV}−OOH are distinguishable as the Mn^{IV}−OOH, and Mn^{IV}−OH contains several LMCT bands compared to others. The Mn^{IV}=O spectrum computed reveals a mixture of d-d and LMCT, and these observations are consistent with similar species reported in the literature.[61] Furthermore, the computed EPR parameters are also in line with the earlier Mn^{IV}=O/OH species with slightly different ligand backbone, offering confidence in the chosen methodology.[60] Among the $S = 3/2$ state of **1a**, **1b**, **2**, and **3** species, the computed NPA charges disclose the largest positive charge in the Mn ion that is located in **1a** followed by **2**, **1b**, and **3** (see Table S5). Similarly, the radical character at the O−O moiety is extremely large for **1a**, whereas a very small spin density is detected for **1b**, **2**, and **3**. Both these quantities are correlated to the electrophilicity of the species and suggest that **1a** is expected to be more reactive than the other species, and this is in agreement with the experimental findings.[21]

Furthermore, EDA reveals that the Mn^{IV}−OOH and Mn^{IV}−OH have similar interaction energy (ΔE_{int}) between
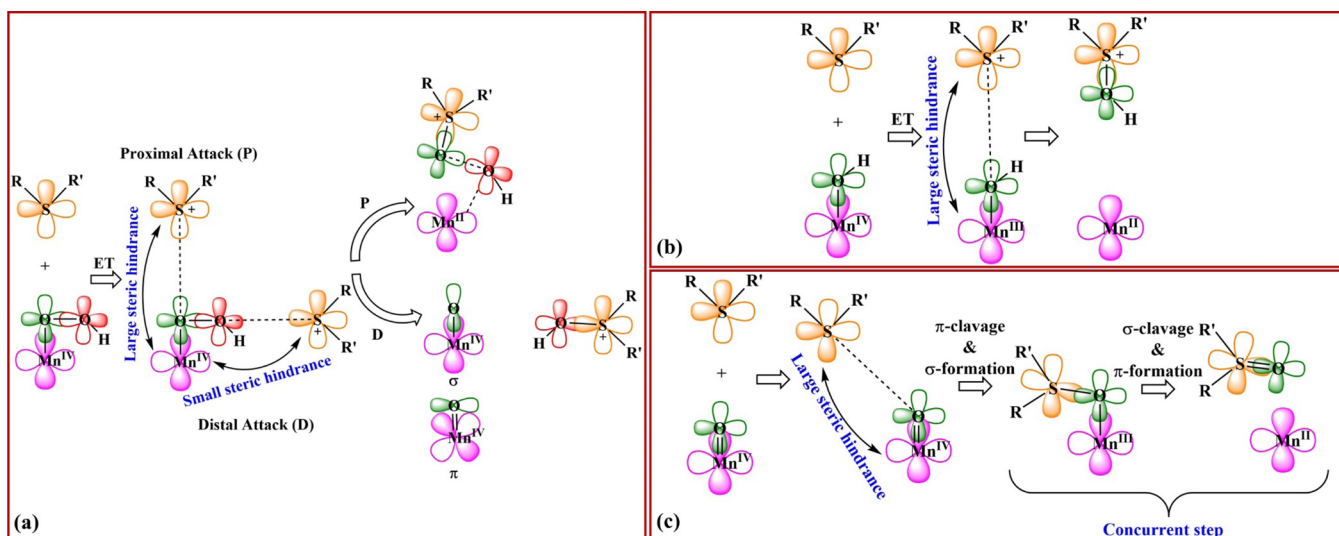
Figure 8. Orbital interaction diagram showing the cleavage and formation of bonds in (a) distal and proximal attacks of $Mn^{IV}-OOH$, (b) $Mn^{IV}-OH$, and (c) $Mn^{IV}=O$.

$\{(Me_2EBC)Mn^{IV}\}$ fragment and $\{X\}$ (here X = $-OOH$ (**1a,1b**) and $-OH$ (**2**)). For species **3**, on the other hand, the ΔE_{int} energy is twice as much as of **1a/1b/2**, and this is due to the $Mn=O$ double bond character (see Table S6). Orbital interaction energy (ΔE_{orb}) and steric energy (ΔE_{steric}) for species **3** are -1640.5 and -2804.5 kJ/mol, and this is two times larger than the estimate obtained for **1a/1b/2**. Among **1a**, **1b**, and **2**, where Mn–O bond is a single bond, ΔE_{int} is found to be **1a** > **2** > **1b**, suggesting stronger Mn–O bond in **1a** than that of **1b** and **2**.

To further understand the nature of electron transfer (ET) from the substrate to the catalyst, we have computed the thermodynamics of ET for all three species, $Mn^{IV}-OOH$, $Mn^{IV}-OH$, and $Mn^{IV}=O$, as shown in Figure 7. These data suggest that the ET from substrate benzyl phenyl sulfide to $Mn^{IV}-OOH$ and $Mn^{IV}-OH$ is feasible as they are strongly exothermic (-130.2 and -146.6 kJ/mol for $Mn^{IV}-OOH$ and $Mn^{IV}-OH$, respectively). On the other hand, the ET in $Mn^{IV}=O$ is an endothermic process with a steep energy penalty of 53.9 kJ/mol energy. It indicates that such a process unlikely occurs here (see Figure 7). The CASSCF/NEVPT2 calculations of one-electron–reduced species of $Mn^{IV}-OOH$ and $Mn^{IV}-OH$ ($Mn^{III}-OOH$ and $Mn^{III}-OH$, see Figure 7) suggest a decrease in the multiconfigurational character upon reduction as the added electron occupies the $\sigma^*_z{}^2$ orbital (see Table S4).

The reactivity of all the species modeled unveils that the reaction occurs at the quartet surface. There are two pathways for the OAT reaction of $Mn^{IV}-OOH$ with benzyl phenyl sulfide involving distal and proximal oxygen atoms. Computed barrier height suggests that the proximal oxygen pathway is unlikely to occur as the kinetic barrier is significantly steeper. The reason is straightforward: the distal oxygen is readily available for the substrate, whereas proximal oxygen is closer to the Mn ion, and this adds a significant steric strain to the transition state. This is reflected in the computed barrier height with the mere 16.5 kJ/mol (24 kJ/mol from the **RC**) for the distal OAT path compared to 115.9 kJ/mol computed for the proximal OAT path.

Furthermore, in the second step of the reaction, $Mn^{IV}=O\cdots$ $[PhCH_2S(OH)Ph]^+$ intermediate forms, which is significantly exothermic. This formation eases out the kinetic requirement for the subsequent reaction facilitating a facile product formation.

Thus, the rate-limiting step is essentially the first step with a barrier height of 16.5 kJ/mol. This barrier height is markedly smaller than many other sulfoxidation reactions reported. For example, $[(TMC)Fe^{III}-OOH]^{2+}$ perform sulfoxidation in S = 5/2 state with the lowest energy barrier of 60.7 kJ/mol,[64] whereas a stronger $[(bispidine)Fe^{IV}=O]^{2+}$ facilitate this transformation with DFT-estimated barrier height of 75.0 kJ/mol.[65] Experimentally, the lowest barrier height estimated for sulfoxidation reaction by $Mn^{IV}=O$ is reported to be 64.8 kJ/mol.[66]

For $Mn^{IV}-OH$ and $Mn^{IV}=O$ species, the computed barriers are 64.5 kJ/mol (137.7 kJ/mol from **RC**) and 56.7 kJ/mol, respectively. Although the barrier for $Mn^{IV}=O$ is not substantial, the formation of **RC** is very stable and enhances the energy penalty for $Mn^{IV}-OH$, rendering this species unreactive toward various substrates even at 50 °C. For species $Mn^{IV}=O$, on the other hand, the barrier computed is not substantial and suggests the possibility of sulfoxidation. As the experimental reactions were carried out at pH level 1.5 for the sulfoxidation reaction, the $Mn^{IV}=O$ species is likely to be protanted, leading to a $Mn^{IV}-OH$ species. This is consistent with earlier reports where $Mn^{IV}=O$ formation was suggested in a basic medium, not in an acidic medium.[21,60,63,67]

To understand the estimated barrier heights further, EDA analysis was performed on the computed transition states. A lower ΔE_{steric} and a larger ΔE_{int} energy were expected to yield a lower barrier height and vice versa.[68,69] Here, the ΔE_{steric} computed for $Mn^{IV}-OOH$, $Mn^{IV}-OH$, and $Mn^{IV}=O$ species are 22.7 kcal/mol, 145.7 kcal/mol, and 118.9 kcal/mol, respectively (see Table S7). The ΔE_{int} for $Mn^{IV}-OOH$, $Mn^{IV}-OH$, and $Mn^{IV}=O$ species at S = 3/2 transition states are -482, -274.5, and -93.3 kJ/mol, respectively (see Table S7). The ΔE_{steric} is exceptionally low in $Mn^{IV}-OOH$ species compared to the other two and contributes significantly to its lower barrier height estimate. The distal oxygen atom lies relatively farther from the Mn center in $Mn^{IV}-OOH$ species than $Mn^{IV}=O$ and $Mn^{IV}-OH$ species, and therefore, the substrate approaches the catalyst much closer. This substantially reduces the steric energy penalty in the hydroperoxo species. As the substrate approaches closer to the oxygen atom, the orbital overlaps are more efficient, leading to a substantial ΔE_{int} energy
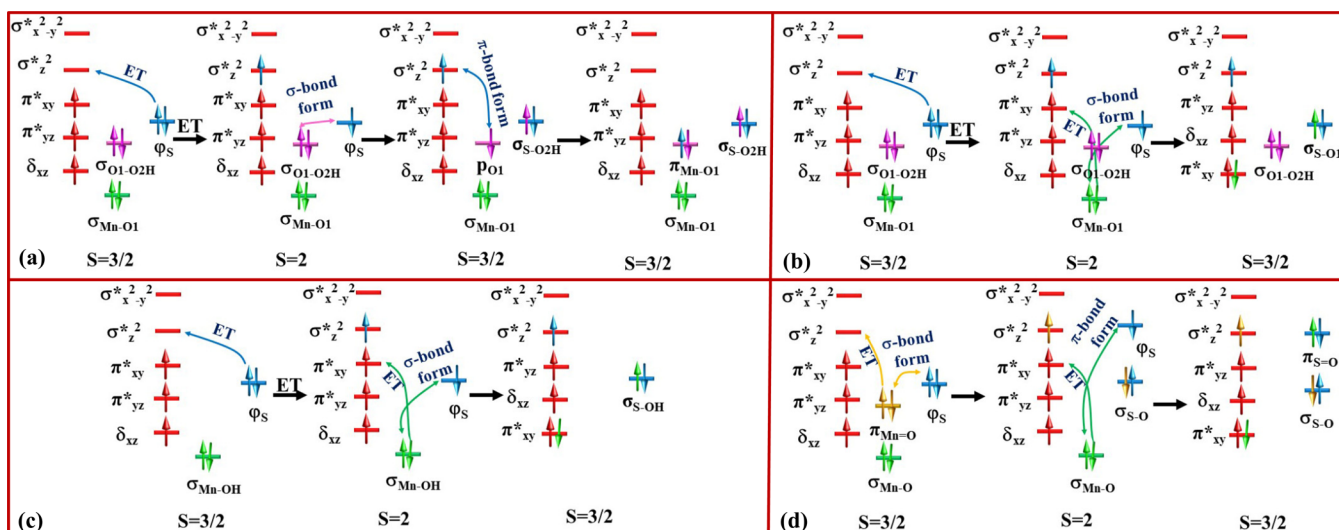
Figure 9. Electron shift diagram showing the cleavage and formation of bonds in (a) distal and (b) proximal attacks of $Mn^{IV}-OOH$, (c) $Mn^{IV}-OH$, and (d) $Mn^{IV}=O$ species.

for $Mn^{IV}-OOH$ species compared to $Mn^{IV}-OH$ and $Mn^{IV}=O$ species. This leads to a very small barrier height for this species in general.

Following the IRC of the $S = 3/2$ transition states corresponding to $Mn^{IV}-OOH$ species compared to $Mn^{IV}-OH$ and $Mn^{IV}=O$ species suggests that distal oxygen pathway, proximal oxygen pathway of $Mn^{IV}-OOH$ species, and $Mn^{IV}-OH$ species follow an ET mechanism, wherein one-electron–reduced Mn^{III} species is stabilized prior to the O–S bond formation. For $Mn^{IV}=O$, on the other hand, the reaction was found to occur in one step with a concurrent reduction to Mn^{II} with the O–S formation (as shown in Figure S5). A plausible ET mechanism is postulated for $Mn^{IV}-OOH$ species as the sulfur cation radical forms during the reaction. This is due to the incorporation of oxygen from water and the formation of minor C–S bond cleavage products in NMR. Furthermore, the observation of kinetic isotopic effect (KIE) of 1.2 for the OAT reaction with $Mn^{IV}-OOH$ correlated with the highly bent nature of the transition state, and in our calculations, the transition state in question is found to have an Mn–O–O bond angle of 118.8°, and this is also consistent with the experimental suggestions. Similarly, for $Mn^{IV}=O$ species, a concerted OAT has been proposed, and this is well established for other ligand architectures.[70] Both these points support our mechanistic findings.

From the orbital interaction and electron shift diagram (see Figures 8a and 9a,b), the ET from RSR' to $Mn^{IV}-OOH$ leads to the formation of $Mn^{III}-OOH$ and $[RSR']^{•+}$ in both proximal and distal attacks. For distal attack, the σ_x O–O bond of $Mn^{III}-OOH$ is cleaving homolytically to individual p_x orbital on each oxygen atom and interacts with the sulfur radical cation p_x orbital to form σ_x bonding $[HO-S(R)(R')]^+$. The left p_x orbital on proximal oxygen makes π_{xy} double bond with d_{xy} orbital of Mn to form a stable species $Mn^{IV}=O$ species (see Figures 8a and 9a,b and Figures S8 and S9). This provides extra stability and lower barrier height for this pathway.

The main reason for the reactivity difference between the $Mn^{IV}-OOH$, $Mn^{IV}-OH$, and $Mn^{IV}=O$ lies in sterics. In $Mn^{IV}-OOH$ species, the O–O bond has to break, whereas in $Mn^{IV}-OH$ and $Mn^{IV}=O$ species, the Mn–O bond has to break. The O–O bond cleavage is energetically less demanding than Mn–

O bond cleavage. In terms of the orbital interaction diagram, $Mn^{IV}-OH$ undergoes an ET process and forms $Mn^{III}-OH$ species (see Figure 8b) with a short Mn–O distance (1.786 Å for **2′**) and hence difficult to approach for the substrate compared to $Mn^{IV}-OH$ species. Borovik and co-workers reported that $Mn^{III}-OH$ species are stable and often unreactive, which supports our findings that $Mn^{IV}-OH$ is significantly less reactive for OAT.[71–75] However, if the mechanism is via HAT or concerted OAT, the reaction is expected to be facile. This is in accordance with OAT reactions observed with substrates such as phosphine with $Mn^{IV}-OH$ species.[70,76] In the sulfoxiation reaction studied, the ET pathway is observed where a strong σ bond is formed between $d_{x^2-y^2}$ (Mn) and p_x (O) atoms (see Figures 8b and 9c and Figure S10) in the $Mn^{III}-OH$ species. This bond has to be cleaved for the OAT reaction to occur, and this enhances the energy penalty suggesting sluggish/no reactivity for this catalyst as observed in the experiments.[21]

The $Mn^{IV}=O$ species also has a large barrier, and this is essentially due to a strong Mn=O bond which has to cleave for the OAT reaction to occur (see Figures 8c and 9d). As Mn=O is a double bond, the π-bond cleaves at the transition state, and the oxygen p_x orbital overlaps with the sulfur atom, drawing a partial bond (see Figure S11). As the Mn–O σ bond is still intact, the Mn–O bond is elongated marginally (0.155 Å) at the transition state compared to an elongation of 0.328 Å in $Mn^{IV}-OH$ species, offering a significant steric strain for the substrate (see Figures 8c and 9d). This places the barrier for this species to be higher than the $Mn^{IV}-OH$ species; however, the computed barrier heights are relatively smaller. This is due to the adaption of a concerted mechanism with a two-electron reduction of $Mn^{IV}=O$, leading to a relatively stable Mn^{II} species. This eases the electronic contribution to the barrier heights and facilitates a relatively faster reaction than $Mn^{IV}-OH$ species. Experimentally, the $Mn^{IV}=O$ species is also found to be unreactive for OAT reactions with alkyl/aromatic sulfides, and this is due to the following: (i) while the kinetic barrier is not substantial, the barrier is twice as high compared to $Mn^{IV}-OOH$ species, and hence, a sluggish reaction is expected and (ii) the reactions were carried out in strongly reducing environment at a pH level of 1.5 where $Mn^{IV}=O$ is likely to get protonated leading to $Mn^{IV}-OH$

species which is unreactive toward alkyl/aromatic sulfides as shown above.

CONCLUSIONS

Here, we have performed the DFT and ab initio DLPNO-CCSD(T) and CASSCF/NEVPT2 calculations to understand the electronic structures of $[(Me_2EBC)Mn^{IV}-OOH]^{3+}(\mathbf{1})$, $[(Me_2EBC)Mn^{IV}-OH]^{3+}(\mathbf{2})$, and $[(Me_2EBC)Mn^{IV}=O]^{2+}(\mathbf{3})$. In addition to this, the mechanism of OAT by these species has been explored. Our key findings are summarized below.

(i) Our DFT as well as DLPNO-CCSD(T) calculations affirm that all the species $Mn^{IV}-OOH$ (**1**), $Mn^{IV}-OH$ (**2**), and $Mn^{IV}=O$ (**3**) have a high-spin ($S = 3/2$) ground state with the excited $S = 1/2$ very high in energy such that the typical two-state reactivity scenario observed in popular $Fe^{IV}=O$ can be ruled out.

(ii) Multiconfigurational CASSCF calculations on the ground $S = 3/2$ state geometries reveal that species $Mn^{IV}-OOH$ and $Mn^{IV}-OH$ have a strong multiconfigurational character with several excited $S = 3/2$ states close-lying leading to a multistate reactivity that does not demand a spin inversion. Species $Mn^{IV}=O$, on the other hand, has a dominant single-reference character and is shown to react via the $S = 3/2$ state. This is different from other $Mn^{IV}=O$ species, which are strongly multiconfigurational in character and perhaps hold the clue on relatively sluggish reactivity of this species toward OAT reactions.

(iii) The OAT reaction of $Mn^{IV}-OOH$ species with alkyl/aromatic sulfides suggests that the reaction proceeds via an ET mechanism with the distal OAT pathway computed to be lowest in energy (16.5 vs 115.9 kJ/mol for proximal attack). The mechanistic findings are in agreement with experiments.

(iv) The OAT transfer reaction in $Mn^{IV}-OH$ proceeds via an ET pathway leading to a stable $Mn^{III}-OH$ species with a net barrier height of 137.7 kJ/mol, whereas species $Mn^{IV}=O$ obeys a concerted mechanism with a barrier height of 57.7 kJ/mol. Both the values are much larger than the $Mn^{IV}-OOH$ species, rationalizing the absence of any reactivity of these species toward the substrates tested.

To this end, our combined DFT and ab initio study unveils the puzzling higher reactivity of $Mn^{IV}-OOH$ species compared to the popular $Mn^{IV}=O$ and $Mn^{IV}-OH$ species. It is apparent that the O–O bond cleavage is more favorable than Mn–O bond breaking and this is also contrary to the trend known in high-valent iron-oxo chemistry, suggesting a greater implication of the mechanistic findings to other metal-oxo catalysts and PSII.

ASSOCIATED CONTENT

Ⓢⓘ Supporting Information

The Supporting Information is available free of charge at https://pubs.acs.org/doi/10.1021/acs.inorgchem.1c01306.

The molecular geometries and electronic energies of all species computed along with spin-density/geometrical parameters and coordinates are available (PDF)

AUTHOR INFORMATION

Corresponding Author

Gopalan Rajaraman − *Department of Chemistry, Indian Institute of Technology Bombay, Mumbai 400076, India;* ⓘ orcid.org/0000-0001-6133-3026; Email: rajaraman@chem.iitb.ac.in

Authors

Ravi Kumar − *Department of Chemistry, Indian Institute of Technology Bombay, Mumbai 400076, India;* ⓘ orcid.org/0000-0001-8465-3495

Bhawana Pandey − *Department of Chemistry, Indian Institute of Technology Bombay, Mumbai 400076, India*

Akta Singh − *Department of Chemistry, Indian Institute of Technology Bombay, Mumbai 400076, India*

Complete contact information is available at:
https://pubs.acs.org/10.1021/acs.inorgchem.1c01306

Notes

The authors declare no competing financial interest.

REFERENCES

(1) Yachandra, V. K.; Sauer, K.; Klein, M. P. Manganese cluster in photosynthesis: where plants oxidize water to dioxygen. *Chem. Rev.* **1996**, *96*, 2927−2950.

(2) Nick, R. J.; Ray, G. B.; Fish, K. M.; Spiro, T. G.; Groves, J. T. Evidence for a weak Mn: O bond and a non-porphyrin radical in manganese-substituted horseradish peroxidase compound I. *J. Am. Chem. Soc.* **1991**, *113*, 1838−1840.

(3) Pecoraro, V. L.; Baldwin, M. J.; Gelasco, A. Interaction of manganese with dioxygen and its reduced derivatives. *Chem. Rev.* **1994**, *94*, 807−826.

(4) Burger, R. M., Nature of activated bleomycin. *Metal-Oxo and Metal-Peroxo Species in Catalytic Oxidations* **2000**, 287−303, DOI: 10.1007/3-540-46592-8_10.

(5) Karlsson, A.; Parales, J. V.; Parales, R. E.; Gibson, D. T.; Eklund, H.; Ramaswamy, S. Crystal structure of naphthalene dioxygenase: side-on binding of dioxygen to iron. *Science* **2003**, *299*, 1039−1042.

(6) Lee, D.; Lippard, S. J. 8.13- Nonheme Di-iron Enzymes. In *Comprehensive Coordination Chemistry II*; McCleverty, J. A.; Meyer, T. J., Eds.; Pergamon: Oxford, 2003, pp 309−342.

(7) Du Bois, J.; Mizoguchi, T. J.; Lippard, S. J. Understanding the dioxygen reaction chemistry of diiron proteins through synthetic modeling studies. *Coord. Chem. Rev.* **2000**, 443−485.

(8) Guo, M.; Lee, Y.-M.; Fukuzumi, S.; Nam, W. Biomimetic metal-oxidant adducts as active oxidants in oxidation reactions. *Coord. Chem. Rev.* **2021**, *435*, No. 213807.

(9) Kumar, R.; Pandey, B.; Sen, A.; Ansari, M.; Sharma, S.; Rajaraman, G. Role of oxidation state, ferryl-oxygen, and ligand architecture on the reactivity of popular high-valent FeIV= O species: A theoretical perspective. *Coord. Chem. Rev.* **2020**, *419*, No. 213397.

(10) Park, M. J.; Lee, J.; Suh, Y.; Kim, J.; Nam, W. Reactivities of mononuclear non-heme iron intermediates including evidence that iron (III)− hydroperoxo species is a sluggish oxidant. *J. Am. Chem. Soc.* **2006**, *128*, 2630−2634.

(11) MacBeth, C. E.; Golombek, A. P.; Young, V. G.; Yang, C.; Kuczera, K.; Hendrich, M. P.; Borovik, A. O2 activation by nonheme iron complexes: a monomeric Fe (III)-oxo complex derived from O2. *Science* **2000**, *289*, 938−941.

(12) Lacy, D. C.; Gupta, R.; Stone, K. L.; Greaves, J.; Ziller, J. W.; Hendrich, M. P.; Borovik, A. S. Formation, Structure, and EPR Detection of a High Spin FeIV— Oxo Species Derived from Either an FeIII— Oxo or FeIII— OH Complex. *J. Am. Chem. Soc.* **2010**, *132*, 12188—12190.

(13) Rohde, J.-U.; In, J.-H.; Lim, M. H.; Brennessel, W. W.; Bukowski, M. R.; Stubna, A.; Münck, E.; Nam, W.; Que, L. Crystallographic and spectroscopic characterization of a nonheme Fe (IV)=O complex. *Science* **2003**, *299*, 1037—1039.

(14) Lyakin, O. Y.; Bryliakov, K. P.; Britovsek, G. J. P.; Talsi, E. P. EPR spectroscopic trapping of the active species of nonheme iron-catalyzed oxidation. *J. Am. Chem. Soc.* **2009**, *131*, 10798—10799.

(15) Jin, N.; Groves, J. T. Unusual kinetic stability of a ground-state singlet oxomanganese (V) porphyrin. Evidence for a spin state crossing effect. *J. Am. Chem. Soc.* **1999**, *121*, 2923—2924.

(16) Jaccob, M.; Ansari, A.; Pandey, B.; Rajaraman, G. Theoretical studies on concerted versus two steps hydrogen atom transfer reaction by non-heme Mn IV/III [double bond, length as m-dash] O complexes: how important is the oxo ligand basicity in the C—H activation step? *Dalton Trans.* **2013**, *42*, 16518—16526.

(17) Mukhopadhyay, S.; Mandal, S. K.; Bhaduri, S.; Armstrong, W. H. Manganese clusters with relevance to photosystem II. *Chem. Rev.* **2004**, *104*, 3981—4026.

(18) Ludwig, M. L.; Metzger, A. L.; Pattridge, K. A.; Stallings, W. C. Manganese superoxide dismutase from Thermus thermophilus: a structural model refined at 1.8 Å resolution. *J. Mol. Biol.* **1991**, *219*, 335—358.

(19) Lovell, T.; Himo, F.; Han, W.-G.; Noodleman, L. Density functional methods applied to metalloenzymes. *Coord. Chem. Rev.* **2003**, *238-239*, 211—232.

(20) Yin, G. Understanding the oxidative relationships of the metal oxo, hydroxo, and hydroperoxide intermediates with manganese (IV) complexes having bridged cyclams: Correlation of the physicochemical properties with reactivity. *Acc. Chem. Res.* **2013**, *46*, 483—492.

(21) Wang, Y.; Shi, S.; Zhu, D.; Yin, G. The oxidative properties of a manganese (IV) hydroperoxide moiety and its relationships with the corresponding manganese (IV) oxo and hydroxo moieties. *Dalton Trans.* **2012**, *41*, 2612—2619.

(22) Frisch, M. J.; Trucks, G. W.; Schlegel, H. B.; Scuseria, G. E.; Robb, M. A.; Cheeseman, J. R.; Scalmani, G.; Barone, V.; Petersson, G. A.; Nakatsuji, H.; Li, X.; Caricato, M.; Marenich, A. V.; Bloino, J.; Janesko, B. G.; Gomperts, R.; Mennucci, B.; Hratchian, H. P.; Ortiz, J. V.; Izmaylov, A. F.; Sonnenberg, J. L.; Williams; Ding, F.; Lipparini, F.; Egidi, F.; Goings, J.; Peng, B.; Petrone, A.; Henderson, T.; Ranasinghe, D.; Zakrzewski, V. G.; Gao, J.; Rega, N.; Zheng, G.; Liang, W.; Hada, M.; Ehara, M.; Toyota, K.; Fukuda, R.; Hasegawa, J.; Ishida, M.; Nakajima, T.; Honda, Y.; Kitao, O.; Nakai, H.; Vreven, T.; Throssell, K.; Montgomery, Jr., J. A.; Peralta, J. E.; Ogliaro, F.; Bearpark, M. J.; Heyd, J. J.; Brothers, E. N.; Kudin, K. N.; Staroverov, V. N.; Keith, T. A.; Kobayashi, R.; Normand, J.; Raghavachari, K.; Rendell, A. P.; Burant, J. C.; Iyengar, S. S.; Tomasi, J.; Cossi, M.; Millam, J. M.; Klene, M.; Adamo, C.; Cammi, R.; Ochterski, J. W.; Martin, R. L.; Morokuma, K.; Farkas, O.; Foresman, J. B.; Fox, D. J. *Gaussian 09 Revision A.02.* Gaussian, Inc.: Wallingford, CT, 2009.

(23) Neese, F. The ORCA program system. *WIREs. Comput. Mol. Sci.* **2012**, *2*, 73—78.

(24) Neese, F. Software update: the ORCA program system, version 4.0. *WIREs. Comput. Mol. Sci.* **2018**, *8*, No. e1327.

(25) Grimme, S. Semiempirical GGA-type density functional constructed with a long-range dispersion correction. *J. Comput. Chem.* **2006**, *27*, 1787—1799.

(26) Hay, P. J.; Wadt, W. R. Ab initio effective core potentials for molecular calculations. Potentials for the transition metal atoms Sc to Hg. *J. Chem. Phys.* **1985**, *82*, 270—283.

(27) Wadt, W. R.; Hay, P. J. Ab initio effective core potentials for molecular calculations. Potentials for main group elements Na to Bi. *J. Chem. Phys.* **1985**, *82*, 284—298.

(28) Hay, P. J.; Wadt, W. R. Ab initio effective core potentials for molecular calculations. Potentials for K to Au including the outermost core orbitals. *J. Chem. Phys.* **1985**, *82*, 299—310.

(29) Ditchfield, R.; Hehre, W. J.; Pople, J. A. Self-consistent molecular-orbital methods. IX. An extended Gaussian-type basis for molecular-orbital studies of organic molecules. *J. Chem. Phys.* **1971**, *54*, 724—728.

(30) Schäfer, A.; Huber, C.; Ahlrichs, R. Fully optimized contracted Gaussian basis sets of triple zeta valence quality for atoms Li to Kr. *J. Chem. Phys.* **1994**, *100*, 5829—5835.

(31) Schäfer, A.; Horn, H.; Ahlrichs, R. Fully optimized contracted Gaussian basis sets for atoms Li to Kr. *J. Chem. Phys.* **1992**, *97*, 2571—2577.

(32) Zhurko, G.; Zhurko, D. ChemCraft, version 1.6. URL: http://www.chemcraftprog.com, 2009.

(33) Mennucci, B. Polarizable continuum model. *WIREs. Comput. Mol. Sci.* **2012**, *2*, 386—404.

(34) Ansari, A.; Kaushik, A.; Rajaraman, G. Mechanistic Insights on the ortho-Hydroxylation of Aromatic Compounds by Non-heme Iron Complex: A Computational Case Study on the Comparative Oxidative Ability of Ferric-Hydroperoxo and High-Valent FeIV=O and FeV=O Intermediates. *J. Am. Chem. Soc.* **2013**, *135*, 4235—4249.

(35) Sen, A.; Vyas, N.; Pandey, B.; Rajaraman, G. Deciphering the mechanism of oxygen atom transfer by non-heme Mn IV—oxo species: an ab initio and DFT exploration. *Dalton Trans.* **2020**, *49*, 10380—10393.

(36) Sen, A.; Vyas, N.; Pandey, B.; Jaccob, M.; Rajaraman, G. Mechanistic Insights on the Formation of High-Valent MnIII/IV=O Species Using Oxygen as Oxidant: A Theoretical Perspective. *Isr. J. Chem.* **2020**, *60*, 973—986.

(37) Pandey, B.; Ansari, A.; Vyas, N.; Rajaraman, G. Structures, bonding and reactivity of iron and manganese high-valent metal-oxo complexes: A computational investigation. *J. Chem. Sci.* **2015**, *127*, 343—352.

(38) Hay, M. A.; Sarkar, A.; Marriott, K. E. R.; Wilson, C.; Rajaraman, G.; Murrie, M. Investigation of the magnetic anisotropy in a series of trigonal bipyramidal Mn (II) complexes. *Dalton Trans.* **2019**, *48*, 15480—15486.

(39) Kumar, R.; Pandey, B.; Rajaraman, G. Comparative oxidative ability of iron (III)-iodosylarene vs. high-valent iron (IV/V)-oxo species: Is lower oxidation state a key to enhance selectivity in organic transformations? *J. Indian Chem. Soc.* **2019**, *96*, 825—836.

(40) Kumar, R.; Katari, M.; Choudhary, A.; Rajaraman, G.; Ghosh, P. Computational insight into the hydroamination of an activated olefin, as catalyzed by a 1, 2, 4-triazole-derived nickel (II) N-heterocyclic carbene complex. *Inorg. Chem.* **2017**, *56*, 14859—14869.

(41) Kumar, R.; Ansari, A.; Rajaraman, G. Axial vs. Equatorial Ligand Rivalry in Controlling the Reactivity of Iron (IV)-Oxo Species: Single-State vs. Two-State Reactivity. *Chem. — Eur. J.* **2018**, *24*, 6818—6827.

(42) Ansari, A.; Ansari, M.; Singha, A.; Rajaraman, G. Interplay of Electronic Cooperativity and Exchange Coupling in Regulating the Reactivity of Diiron (IV)-oxo Complexes towards C—H and O—H Bond Activation. *Chem. — Eur. J.* **2017**, *23*, 10110—10125.

(43) Ansari, M.; Senthilnathan, D.; Rajaraman, G. Deciphering the origin of million-fold reactivity observed for the open core diiron [HO—Fe III—O—Fe IV [double bond, length as m-dash] O] 2+ species towards C—H bond activation: role of spin-states, spin-coupling, and spin-cooperation. *Chem. Sci.* **2020**, *11*, 10669—10687.

(44) Atanasov, M.; Comba, P.; Martin, B.; Müller, V.; Rajaraman, G.; Rohwer, H.; Wunderlich, S. DFT models for copper (II) bispidine complexes: Structures, stabilities, isomerism, spin distribution, and spectroscopy. *J. Comput. Chem.* **2006**, *27*, 1263—1277.

(45) Verma, P.; Varga, Z.; Klein, J. E. M. N.; Cramer, C. J.; Que, L.; Truhlar, D. G. Assessment of electronic structure methods for the determination of the ground spin states of Fe (II), Fe (III) and Fe (IV) complexes. *Phys. Chem. Chem. Phys.* **2017**, *19*, 13049—13069.

(46) Swart, M.; Gruden, M. Spinning around in transition-metal chemistry. *Acc. Chem. Res.* **2016**, *49*, 2690—2697.

(47) Neese, F. Theoretical spectroscopy of model-nonheme [Fe (IV) OLS] 2+ complexes in their lowest triplet and quintet states using multireference ab initio and density functional theory methods. *J. Inorg. Biochem.* **2006**, *100*, 716−726.

(48) Geng, C.; Ye, S.; Neese, F. Analysis of reaction channels for alkane hydroxylation by nonheme iron (IV)−oxo complexes. *Angew. Chem., Int. Ed.* **2010**, *49*, 5717−5720.

(49) Acuña-Parés, F.; Costas, M.; Luis, J. M.; Lloret-Fillol, J. Theoretical study of the water oxidation mechanism with non-heme Fe (Pytacn) iron complexes. Evidence that the FeIV (O)(Pytacn) species cannot react with the water molecule to form the O−O bond. *Inorg. Chem.* **2014**, *53*, 5474−5485.

(50) Comba, P.; Faltermeier, D.; Krieg, S.; Martin, B.; Rajaraman, G. Spin state and reactivity of iron (IV) oxido complexes with tetradentate bispidine ligands. *Dalton Trans.* **2020**, *49*, 2888−2894.

(51) Neale, S. E.; Pantazis, D. A.; Macgregor, S. A. Accurate computed spin-state energetics for Co (III) complexes: implications for modelling homogeneous catalysis. *Dalton Trans.* **2020**, *49*, 6478−6487.

(52) Weigend, F.; Ahlrichs, R. Balanced basis sets of split valence, triple zeta valence and quadruple zeta valence quality for H to Rn: Design and assessment of accuracy. *Phys. Chem. Chem. Phys.* **2005**, *7*, 3297−3305.

(53) van Wüllen, C. Molecular density functional calculations in the regular relativistic approximation: Method, application to coinage metal diatomics, hydrides, fluorides and chlorides, and comparison with first-order relativistic calculations. *J. Chem. Phys.* **1998**, *109*, 392−399.

(54) Glendening, E.; Reed, A.; Carpenter, J.; Weinhold, F. *NBO, version 3.1.* Gaussian, Inc.: Pittsburgh, PA, 2003.

(55) Foster, J. P.; Weinhold, F. Natural hybrid orbitals. *J. Am. Chem. Soc.* **1980**, *102*, 7211−7218.

(56) Gorelsky, S. *AOMix: Program for molecular orbital analysis*, 1997.

(57) Our attempt to obtain electronically correct $^4\mathbf{1a_{is,u}}$ did not succeed as it converges to $^4\mathbf{1a_{hs,d}}$ species.

(58) Rice, D. B.; Massie, A. A.; Jackson, T. A. Experimental and Multireference ab Initio Investigations of Hydrogen-Atom-Transfer Reactivity of a Mononuclear MnIV-oxo Complex. *Inorg. Chem.* **2019**, *58*, 13902−13916.

(59) Neu, H. M. *Modulating Dioxygen Activation and Oxygen Atom Transfer Reactivity of Manganese Corrolazines.* Johns Hopkins University, 2015.

(60) Leto, D. F.; Massie, A. A.; Colmer, H. E.; Jackson, T. A. X-Band electron paramagnetic resonance comparison of mononuclear MnIV-oxo and MnIV-hydroxo complexes and quantum chemical investigation of MnIV zero-field splitting. *Inorg. Chem.* **2016**, *55*, 3272−3282.

(61) Saisaha, P.; de Boer, J. W.; Browne, W. R. Mechanisms in manganese catalysed oxidation of alkenes with H_2O_2. *Chem. Soc. Rev.* **2013**, *42*, 2059−2074.

(62) Please note that the PCd species are not fully optimized and are only obtained directly from IRC coordinate analysis. Although the frequency calculations reveal all positive frequencies for these species, full geometry optimization does not results in a product complex where both the MnIII-OH and the substrates are weakly bound.

(63) Leto, D. F.; Massie, A. A.; Rice, D. B.; Jackson, T. A. Spectroscopic and computational investigations of a mononuclear manganese (IV)-oxo complex reveal electronic structure contributions to reactivity. *J. Am. Chem. Soc.* **2016**, *138*, 15413−15424.

(64) Kim, Y. M.; Cho, K.-B.; Cho, J.; Wang, B.; Li, C.; Shaik, S.; Nam, W. A mononuclear non-heme high-spin iron (III)−hydroperoxo complex as an active oxidant in sulfoxidation reactions. *J. Am. Chem. Soc.* **2013**, *135*, 8838−8841.

(65) Jaccob, M.; Comba, P.; Maurer, M.; Vadivelu, P.; Venuvanalingam, P. A combined experimental and computational study on the sulfoxidation by high-valent iron bispidine complexes. *Dalton Trans.* **2011**, *40*, 11276−11281.

(66) Singh, P.; Stewart-Jones, E.; Denler, M. C.; Jackson, T. A. Mechanistic insight into oxygen atom transfer reactions by mononuclear manganese (iv)−oxo adducts. *Dalton Trans.* **2021**, *50*, 3577−3585.

(67) Mallick, D.; Shaik, S. Theory Revealing Unusual Non-Rebound Mechanisms Responsible for the Distinct Reactivities of O═MnIV═O and [HO−MnIV−OH] 2+ in C−H Bond Activation. *ACS Catal.* **2016**, *6*, 2877−2888.

(68) Guo, M.; Corona, T.; Ray, K.; Nam, W. Heme and nonheme high-valent iron and manganese oxo cores in biological and abiological oxidation reactions. *ACS Cent. Sci.* **2019**, *5*, 13−28.

(69) Usharani, D.; Lacy, D. C.; Borovik, A. S.; Shaik, S. Dichotomous hydrogen atom transfer vs proton-coupled electron transfer during activation of X−H bonds (X= C, N, O) by nonheme iron−oxo complexes of variable basicity. *J. Am. Chem. Soc.* **2013**, *135*, 17090−17104.

(70) Xu, A.; Xiong, H.; Yin, G. Distinct oxygenation difference between manganese (IV) hydroxo and oxo moieties: Electron transfer versus concerted oxygen transfer. *Chem. − Eur. J.* **2009**, *15*, 11478−11481.

(71) Gupta, R.; Borovik, A. S. Monomeric MnIII/II and FeIII/II complexes with terminal hydroxo and oxo ligands: probing reactivity via O−H bond dissociation energies. *J. Am. Chem. Soc.* **2003**, *125*, 13234−13242.

(72) Park, Y. J.; Ziller, J. W.; Borovik, A. S. The effects of redox-inactive metal ions on the activation of dioxygen: isolation and characterization of a heterobimetallic complex containing a MnIII−(μ-OH)−CaII core. *J. Am. Chem. Soc.* **2011**, *133*, 9258−9261.

(73) Taguchi, T.; Stone, K. L.; Gupta, R.; Kaiser-Lassalle, B.; Yano, J.; Hendrich, M. P.; Borovik, A. S. Preparation and properties of an Mn IV−hydroxide complex: proton and electron transfer at a mononuclear manganese site and its relationship to the oxygen evolving complex within photosystem II. *Chem. Sci.* **2014**, *5*, 3064−3071.

(74) Gupta, R.; Taguchi, T.; Borovik, A. S.; Hendrich, M. P. Characterization of monomeric MnII/III/IV−hydroxo complexes from X-and Q-band dual mode electron paramagnetic resonance (EPR) spectroscopy. *Inorg. Chem.* **2013**, *52*, 12568−12575.

(75) Gupta, R.; MacBeth, C. E.; Young, V. G.; Borovik, A. S. Isolation of monomeric MnIII/II− OH and MnIII−O complexes from water: evaluation of O−H bond dissociation energies. *J. Am. Chem. Soc.* **2002**, *124*, 1136−1137.

(76) Lee, Y.-M.; Yoo, M.; Yoon, H.; Li, X.-X.; Nam, W.; Fukuzumi, S. Direct oxygen atom transfer versus electron transfer mechanisms in the phosphine oxidation by nonheme Mn (iv)-oxo complexes. *Chem. Commun.* **2017**, *53*, 9352−9355.

■ **NOTE ADDED AFTER ASAP PUBLICATION**

This paper was published on the Web on July 22, 2021. Additional text corrections were implemented, and the corrected version was reposted on July 23, 2021.